How to cite: *Angew. Chem. Int. Ed.* **2020**, *59*, 22756–22762
International Edition: doi.org/10.1002/anie.202011802
German Edition: doi.org/10.1002/ange.202011802

Gas Separation

Tuning Gate-Opening of a Flexible Metal–Organic Framework for Ternary Gas Sieving Separation

Qiubing Dong[+], Xin Zhang[+], Shuang Liu[+], Rui-Biao Lin, Yanan Guo, Yunsheng Ma, Akira Yonezu, Rajamani Krishna, Gongpin Liu, Jingui Duan, Ryotaro Matsuda, Wanqin Jin, and Banglin Chen**

Abstract: *In comparison with the fast development of binary mixture separations, ternary mixture separations are significantly more difficult and have rarely been realized by a single material. Herein, a new strategy of tuning the gate-opening pressure of flexible MOFs is developed to tackle such a challenge. As demonstrated by a flexible framework NTU-65, the gate-opening pressure of ethylene (C_2H_4), acetylene (C_2H_2), and carbon dioxide (CO_2) can be regulated by temperature. Therefore, efficient sieving separation of this ternary mixture was realized. Under optimized temperature, NTU-65 adsorbed a large amount of C_2H_2 and CO_2 through gate-opening and only negligible amount of C_2H_4. Breakthrough experiments demonstrated that this material can simultaneously capture C_2H_2 and CO_2, yielding polymer-grade (>99.99 %) C_2H_4 from single breakthrough separation.*

Introduction

In recent years, researchers have sought for energy-efficient separation technologies using advanced porous adsorbents. As a new type of crystalline material, metal–organic frameworks (MOFs), also known as porous coordination polymers (PCPs), have demonstrated remarkable performance for gas separation thanks to the highly tunable pore size and surface functionality.[1] Flexible MOFs are unique class of MOFs that undergo structural transformation with the variation of guest, pressure or temperature.[2] Gate-opening adsorption of flexible MOF was first discovered in 2003, and the gate-opening pressure was found to be guest dependent.[3] Strong gas-framework interaction usually leads to lower gate-opening pressure since the high adsorption enthalpy of such gas can overcome the energy requirement for the phase transition even at low pressure.[4] For smaller gas molecule, the gate-opening pressure is also lower as smaller degree of structural change is needed to accommodate smaller molecule in the pore.[5] Selective gate-opening adsorption has realized several important binary gas separation[6] with high sieving performance that is comparable to those of rigid sieving MOFs.

Ethylene (C_2H_4) is one of the most essential feedstocks and is widely used to produce polyethylene and other valued products in modern life.[7] Generally, during C_2H_4 production such as oxidative coupling of methane process, acetylene (C_2H_2) and carbon dioxide (CO_2) coexist with C_2H_4.[8] These impurities must be removed to obtain high purity C_2H_4 for polyethylene production. Current purification technologies involve catalytic hydrogenation of C_2H_2 with precious metal catalyst at high temperature and basic solution for CO_2 chemisorption, which require high capital and energy cost.[9] For such ternary mixture, generally C_2H_2 is selectively adsorbed over C_2H_4,[8a,10] while CO_2/C_2H_4 separation is more challenging due to the smaller difference of their quadrupole moments (1.5×10^{-26} esu cm^2 for C_2H_4, 4.3×10^{-26} esu cm^2 for CO_2, and 7.2×10^{-26} esu cm^2 for C_2H_2).[11] Rigid MOFs with strong C_2H_4 binding sites also adsorb CO_2 efficiently. For example, MOF-74 series and M_2(*m*-dobdc) series MOFs with open metal sites efficiently adsorbs both. CO_2 and C_2H_4, which limited the separation performance.[12] Ideally, molecular sieving separation is favorable since the co-adsorption of C_2H_4 is precluded and most of the C_2H_4 in the mixture can be recovered. As most MOFs has certain degree of flexibility by linker rotation and distortion, it is quite challenging to design high sieving MOFs for hydrocarbon separation.[10b,13] Flexible MOFs with controllable gate-opening pressure offers new opportunity for such a challenging separation.

Compared with the binary mixture, separation of ternary or quaternary mixture is more challenging and often requires multiple adsorbents.[9,14] Flexible MOFs through selective gate-opening adsorption have great potential for this goal. For a certain gas, the gate-opening pressure is usually lower at low

---

[*] Q. Dong,[+] Y. Guo, Prof. Dr. G. Liu, Prof. Dr. J. Duan, Prof. Dr. W. Jin
State Key Laboratory of Materials-Oriented Chemical Engineering
College of Chemical Engineering, Nanjing Tech University
Nanjing 211816 (China)
E-mail: duanjingui@njtech.edu.cn

Dr. X. Zhang,[+] Dr. R.-B. Lin, Prof. Dr. B. Chen
Department of Chemistry, University of Texas at San Antonio
One UTSA Circle, San Antonio, TX 78249-0698 (USA)
E-mail: banglin.chen@utsa.edu

S. Liu[+]
School of Chemistry & Chemical Engineering
Shangqiu Normal University
Shangqiu 476000 (China)

Prof. Dr. Y. Ma, A. Yonezu, Prof. Dr. R. Matsuda
Department of Applied Chemistry
Graduate School of Engineering, Nagoya University
Nagoya 464-8603 (Japan)

Prof. Dr. R. Krishna
Van't Hoff Institute for Molecular Sciences, University of Amsterdam
1098 XH Amsterdam (The Netherlands)

[+] These authors contributed equally to this work.

Supporting information and the ORCID identification number(s) for the author(s) of this article can be found under: https://doi.org/10.1002/anie.202011802.

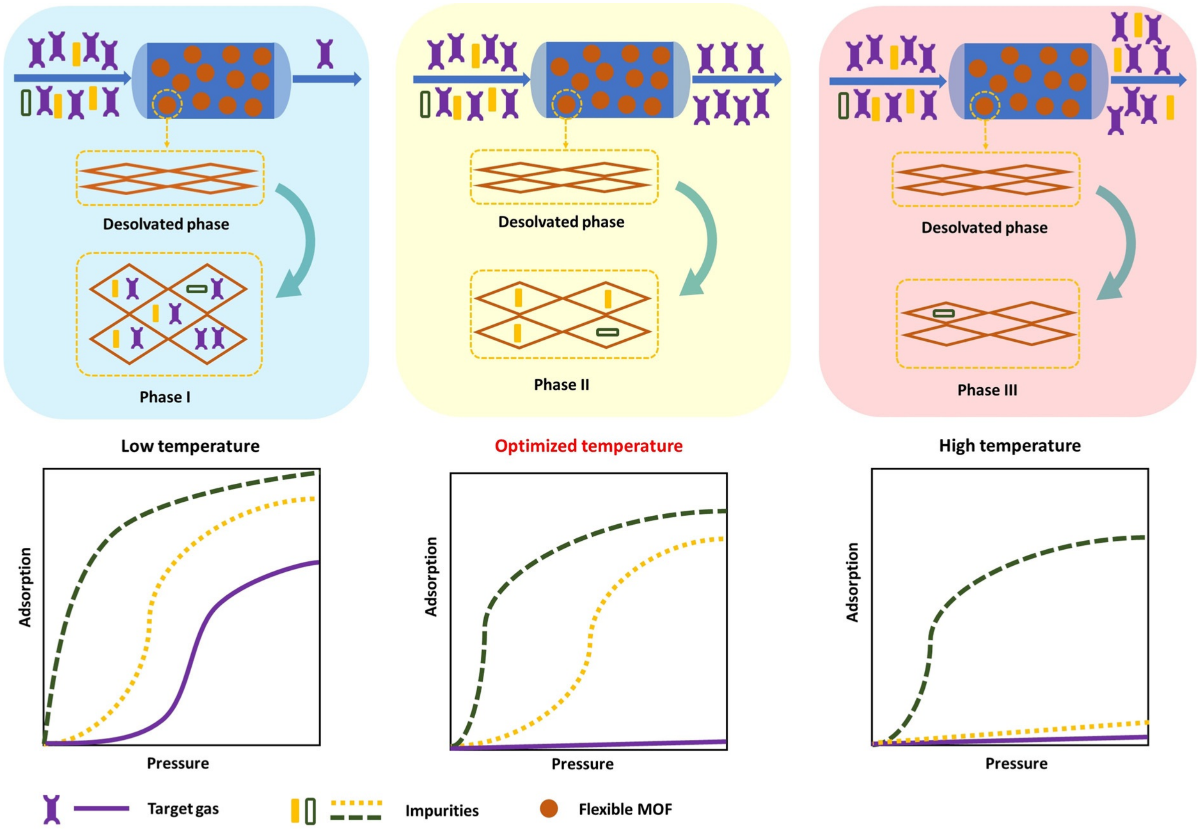

Scheme 1. Illustration of the temperature optimization for ternary mixture separation by flexible MOFs. At low temperature, all three gases can be adsorbed, which lead to co-adsorption of target gas and low productivity. At optimized temperature, two impurities are selectively adsorbed and pure target gas is obtained in high yield. At high temperature, only one type of impurity is adsorbed, therefore the product is not pure.

temperature, because adsorption is an exothermic process and lower temperature is thermodynamically favorable.[15] Therefore, we can regulate the gate-opening pressure by temperature and realize the complete separation of multi-component mixture. For a ternary mixture separation, as shown in Scheme 1, the desolvated flexible framework can adsorb three types of gases through phase transition to more opened structure at very low temperature. As the temperature increases, the gate-opening pressure increases. At certain temperature, the framework adsorbs two impurities of smaller size or with stronger gas–framework interaction and produces desired gas in high purity. At higher temperature, only one impurity can induce the phase transition and be adsorbed, therefore the separation is incomplete. Herein, we demonstrate this strategy with a flexible framework NTU-65 for sieving separation of $C_2H_4/C_2H_2/CO_2$ mixture. At optimized temperature (263 K), NTU-65 adsorbs large amount of C_2H_2 (86.3 $cm^3 g^{-1}$), and CO_2 (79.5 $cm^3 g^{-1}$) through gate-opening process, while only negligible amount of C_2H_4 (2.2 $cm^3 g^{-1}$). As a result, this flexible MOF material captures C_2H_2 and CO_2 exclusively and produces polymer-grade C_2H_4 (> 99.99 %) with very high recovered C_2H_4 percentage from $C_2H_4/C_2H_2/CO_2$ mixture in one step.

Results and Discussion

The reaction of 1,4-di(1*H*-imidazol-1-yl)benzene (**L1**) in DMF and $Cu(SiF_6)\cdot 6H_2O$ in H_2O at room temperature afforded the purple crystals of $[Cu(\mathbf{L1})_2SiF_6]\cdot x$*Solvent* (NTU-65).[16] Single crystal X-ray measurements reveal that NTU-65 crystallizes in a monoclinic space group. The asymmetric unit of NTU-65 includes one Cu^{2+} cation, one SiF_6^{2-} anion, and two **L1** ligands (Figure S1). Each of the ligand and SiF_6^{2-} ions coordinate to two Cu atoms, respectively (Figure 1 a,b). In view of the metal center, the Cu^{2+} cations are octahedrally coordinated by four imidazole N atoms at equatorial positions from four **L1** and two F atoms in axial positions from two SiF_6^{2-} ions (Figure 1 c). Therefore, a three-dimensional (3D) framework with **pcu** topology was established (Supporting Information, Figure S2). The ligands are further connected by multiple hydrogen bonds from all F atoms of the SiF_6^{2-} ion (Supporting Information, Table S2). The NTU-65 framework has cross-linked 2D channels along the *a–c* plane (Supporting Information, Figure S3), which are significantly different from the channels of typical SIFSIX materials (Supporting Information, Figure S4).[6a,17] As a result, two types of channels that feature the rectangular and ultramicroporous window aperture of 2.6×3.4 and 5.2×6.3 Å^2 were observed (Figure 1 d–g).

The phase purity of the bulk crystals was identified by powder X-ray diffraction (PXRD) patterns and LeiBail

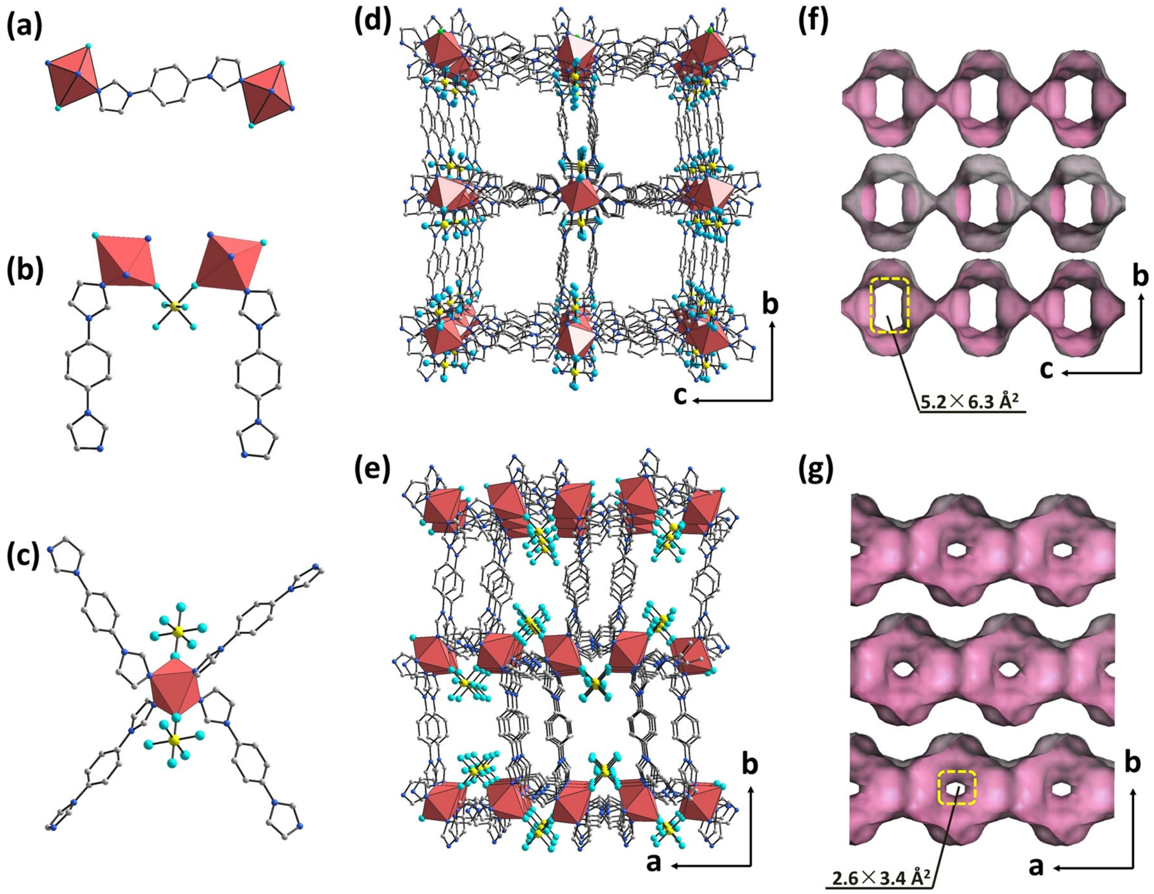

Figure 1. Structure and channel of NTU-65. Coordination configuration of a) **L1**, b) SiF_6^{2-} ion, and c) Cu center. Brown red polyhedron represents octahedrally coordinated Cu atom. d),e) Crystal structure view along *a* and *c* axis. f),g) Channels along a axis and c axis with aperture size of 5.2×6.3 Å^2 and 2.6×3.4 Å^2 respectively. C gray, N blue, F cyan, Si yellow.[27]

fitting (Supporting Information, Figures S5, S6). After exchanging the guest by dry methanol, the fully activated NTU-65 framework was obtained by degassing under high vacuum at 120 °C for 24 hours according to the thermogravimetric (TG) results. PXRD measurement revealed that NTU-65 underwent structural transformation after desolvation (Supporting Information, Figure S5). The activated framework is thermally stable up to 300 °C according to the TG analysis (Supporting Information, Figure S8).

We next evaluated the permanent porosity of NTU-65 by N_2 adsorption at 77 K. A sudden increase of adsorption at pressure of $P/P_0 = 0.12$ was observed indicating a gate-opening process (Supporting Information, Figure S11). In the desorption process, the isotherm showed a certain hysteresis, which is typical for flexible frameworks.[1c,18] Based on the N_2 adsorption isotherm, NTU-65 has a BET (Langmuir) surface area of 680 (1002) m^2 g^{-1} and a pore volume of 0.372 cm^3·g^{-1} (Supporting Information, Figures S12, S13), which is almost same as the calculated values (0.379 cm^3 g^{-1}) from single crystal data. Furthermore, the cavity size distribution (5–6 Å) is also close to the determined values from the crystal structure (Supporting Information, Figure S14). The softness of the framework and the microporous environment prompted us to evaluate the potential of NTU-65 for gas separation. We first measured the C_2H_2 adsorption under the temperature range of 195 to 333 K. As shown in the Supporting Information, Figure S15, the gate-opening pressure increases from 1.2 kPa (263 K) to around 20 kPa (313 K) and 42 kPa (333 K) indicating that the gate-opening pressure is temperature dependent. Such temperature dependent gate-opening has also been observed for CO_2 and C_2H_4 which possess higher gate-opening pressure (Supporting Information, Figures S16, S17). At 298 K, the C_2H_2 adsorption capacity of NTU-65 (3.36 mmol g^{-1}, 75.4 cm^3 g^{-1}) is comparable to that of UTSA-300[6a] (3.41 mmol g^{-1}, 76.4 cm^3 g^{-1}) and SIFSIX-3-Zn[10a] (3.86 mmol g^{-1}, 86.5 cm^3 g^{-1}). Interestingly, only negligible amount of CO_2 (2.3 cm^3 g^{-1}) and C_2H_4 (1.2 cm^3 g^{-1}) can be adsorbed at 298 K showing a guest dependent gate-opening phenomenon (Figure 2 c). The selective gate-opening by C_2H_2 is likely due to strong binding affinity to the framework, as suggested by density functional theory (DFT) calculations. According to the structural model (Supporting Information, Figures S19–S22), we found hydrogen bonds between terminal $\mathbf{H_{C2H2}}$ atoms and the F atoms from SiF_6^{2-} anions ($d_{H\cdots F}$: 1.88 Å and 1.99 Å), and multiple C−H⋯C van der Waals (vdW) interactions between the $\mathbf{C_{C2H2}}$ atoms and adjacent $\mathbf{H_L}$ ($d_{H\cdots C}$: 2.49 to 2.93 Å).

To simultaneously encapsulate the two impurities (C_2H_2 and CO_2) from a ternary mixture, significant CO_2 adsorption is required. Adsorption measurement at 195 K showed

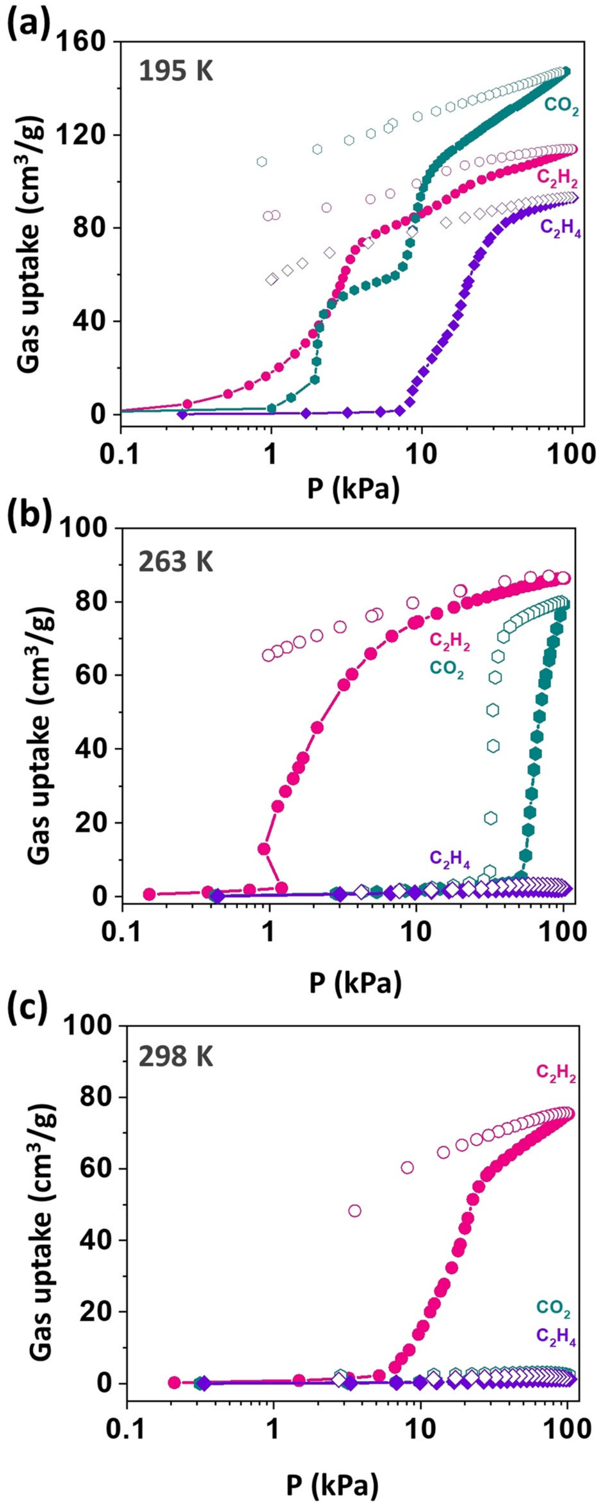

Figure 2. Temperature-dependent adsorption of NTU-65. C_2H_2, C_2H_4, and CO_2 adsorption (solid symbols) and desorption (hollow symbols) isotherms at 195 K (a), 263 K (b), and 298 K (c).

uptake of all three gases (Figure 2a), which is not promising for efficient separation of ternary mixture because the high C_2H_4 uptake would result in significant amount of co-adsorption of C_2H_4 and low percentage of recycled C_2H_4. Since C_2H_4 showed highest gate-opening pressure, it is likely that at some temperature between 195 and 298 K, only C_2H_2 and CO_2 can open the pore and be captured. At 263 K, NTU-65 showed remarkable adsorption of C_2H_2 (86.3 $cm^3\,g^{-1}$) and CO_2 (79.5 $cm^3\,g^{-1}$), and only negligible amount of C_2H_4 (2.2 $cm^3\,g^{-1}$) as shown in Figure 2b. Therefore, it is promising to simultaneously capture C_2H_2 and CO_2 from the ternary mixture of $C_2H_4/C_2H_2/CO_2$ by NTU-65 at 263 K. Adsorption isobar results (Supporting Information, Figure S18) indicated simultaneously high C_2H_2/C_2H_4 and CO_2/C_2H_4 uptake ratios between 250 to 270 K, which further supported our temperature choice.

The structural change during adsorption process was studied by in situ coincident PXRD/sorption measurements during the C_2H_2 adsorption at 189 K and 333 K.[19] As shown in the Supporting Information, Figure S23, we observed two phases transitions at 189 K and one phase transition at 333 K. The phase transition pressure is much higher at 333 K (Supporting Information, Figure S24). These results showed that the phase transition and gate-opening pressure are temperature dependent. Further, the varied cell parameters that determined from synchrotron-based PXRD measurements validate again the phase transitions[20] (Supporting Information, Figures S25–S28, Table S3).

Next, we calculated the amount and percentage of recovered C_2H_4 from binary mixtures of C_2H_2/C_2H_4 and CO_2/C_2H_4 for NTU-65. The percentage of recovered C_2H_4 is defined as amount of recovered pure C_2H_4 divided by the total amount of C_2H_4 in the feed gas mixture. High percentage of recovered C_2H_4 means that most of the valuable C_2H_4 molecules can be recovered from the mixture in a single breakthrough cycle. As shown in Figure 3, the amount of C_2H_4 recycled by NTU-65 from the CO_2/C_2H_4 (75:25, v/v) mixture is quite high compared with some representative zeolite materials in a recent study.[22] At the same time, 99.87 % of the C_2H_4 in the mixture can be recycled thanks to the low C_2H_4 adsorption. Likewise, large amount (3.7 $mmol\,g^{-1}$) and high percentage (97.7 %) of C_2H_4 can be recovered from the C_2H_2/C_2H_4 (50:50, v/v) mixture by NTU-65, which is higher or comparable to the current benchmark materials,[10a,b,21] as shown in the Supporting Information, Figure S29.

Gas separation under dynamic process is important for practical application. Transient breakthrough simulation indicates that NTU-65 would be efficient adsorbent for C_2H_2/C_2H_4 and CO_2/C_2H_4 separations (Supporting Information, Figures S30–S32). Experimental breakthrough was carried out with handmade equipment.[21a,23] The initial activated sample bed was swept by He flow at 100 °C for 8 hours to remove impurities from the system. We first carried out breakthrough experiments with the feed gas of C_2H_2/C_2H_4, where the gas ratio is 1/99 (v/v) at 263 K. (Figure 4a). As expected, C_2H_4 with high purity $>$99.99 % was the first effluent, while C_2H_2 was selectively absorbed by the sample bed with long retained time of about 100 min. After the breakthrough experiment, the sample was regenerated under He flow for 20 min at 358 K which is lower temperature than that of a flexible MOF with open metal site (393 K).[24] Furthermore, same breakthrough curves were observed during the cycling breakthrough experiments (Supporting

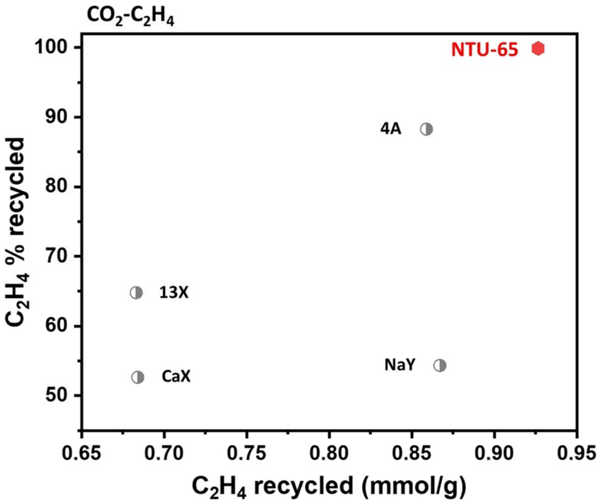

Figure 3. CO_2/C_2H_4 separation performance. Amount and percentage of C_2H_4 recovered from CO_2/C_2H_4 (75:25, v/v) by NTU-65 in comparison with benchmark materials.

Information, Figure S33), indicating the excellent stability and reversible pore opening/closing of NTU-65. The C_2H_2/C_2H_4 separation can also be realized at higher temperature of 298 K and 333 K (Supporting Information, Figure S34–S37). Next, the binary gas separation of CO_2/C_2H_4 (1/9, v/v) was also investigated at 263 K. Likewise, NTU-65 selectively captured CO_2 molecules, and yielded purity C_2H_4 (> 99.99 %) in the outlet of column (Figure 4b). The CO_2/C_2H_4 separation performance was retained during another ten cycling breakthrough experiments (Supporting Information, Figure S38). In light of the excellent separation performance for the binary mixture at 263 K, we then conducted ternary separation of $C_2H_4/C_2H_2/CO_2$ (Figure 4c). After introducing the $C_2H_4/C_2H_2/CO_2$ mixture (90/1/9, v/v/v) inside the system, the effluent of polymer-grade C_2H_4 (> 99.99 %) was detected at 11.2 min, while the outflow of CO_2 and C_2H_2 from the sample bed was around 23.0 min and 174.4 min. The industrial mixtures generally contain 1 % of C_2H_2 and up to about 30 % of CO_2.[10,25] We therefore altered the mixture ratios by tuning CO_2 percentage and kept C_2H_2/C_2H_4 ratio of 1:99. As shown in the Supporting Information, Figure S39 and S40, $C_2H_4/C_2H_2/CO_2$ mixtures with volume ratio of 95.7:0.967:3.33 (v/v/v) and 66.00:0.67:33.33 (v/v/v) can be separated by NTU-65 yielding pure C_2H_4. Low percentage of CO_2 can be efficiently captured. when the CO_2 percentage increased to 33.33 %, the separation performance decreased slightly. These breakthrough experiments demonstrated that NTU-65 maintained the selective adsorption under dynamic process and high purity C_2H_4 can be separated from the ternary mixture in one step.

In comparison with NTU-65, we also measured high-surface-area activated carbon ($S_{BET} \approx 1100\ m^2 g^{-1}$) with no phase transition and a gate-opening MOF ZIF-7[26] (Supporting Information, Figure S7) with two porous phases. The activated carbon material exhibits typical adsorption isotherms of rigid porous materials. The C_2H_4 and C_2H_2 adsorption are very close and higher than CO_2 adsorption at corresponding temperatures (263 K to 318 K; Supporting Information, Figure S41). The corresponding column breakthrough experiments (Supporting Information, Figure S43) showed that C_2H_4 and C_2H_2 are preferably captured and simultaneously broke through, which could not produce pure C_2H_4 like NTU-65. The adsorption isotherms of ZIF-7 showed gate-opening effect for all three gases and C_2H_4 exhibits slightly lower gate-opening pressure than C_2H_2 and CO_2 at different temperatures (263 K to 318 K; Supporting Information, Figure S42). Breakthrough experiments (Supporting Information, Figure S44) showed that C_2H_4 and C_2H_2 eluted out simultaneously at very early stage yielding incomplete separation. The results of activated carbon and ZIF-7 together indicated that a material with temperature-regulated phase transition from less porous phase to open phase might be essential for such separation strategy.

Moreover, NTU-65 also possesses remarkable water/chemical stability. From PXRD analysis, NTU-65 showed the same diffraction and cell parameters after a long-term treatment where the crystals were soaked in water for two months at 298 K (Supporting Information, Figure S45). Furthermore, the crystallinity of NTU-65 retained after immersing the crystal in water of pH 2–12 at 298 K (24 h) and pH 2–7 at 373 K (24 h), as shown in the Supporting Information, Figure S46. More importantly, the N_2 adsorption

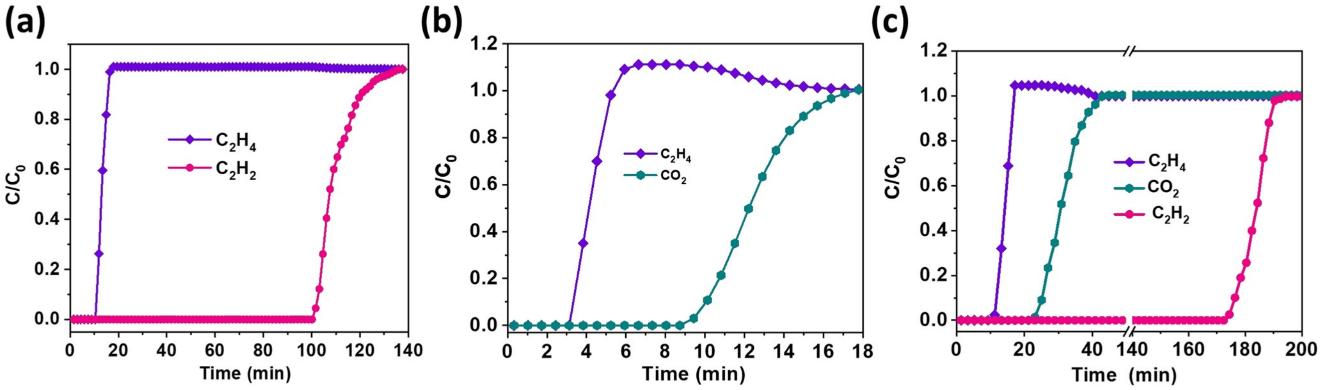

Figure 4. Breakthrough curves of NTU-65 at 263 K. a) Binary mixture separation of C_2H_2/C_2H_4, b) Binary mixture separation of CO_2/C_2H_4. c) Ternary separation of $C_2H_4/C_2H_2/CO_2$ mixture. The total pressure for all experiments is 1 bar, and the gas velocity is 3 mL min^{-1}.

isotherm showed that acid-treated NTU-65 features an almost identical pore opening feature and total pore volume as those with the fresh sample (Supporting Information, Figure S47).

Conclusion

Guest-dependent gate-opening phenomenon of flexible porous MOFs is promising for selective gas adsorption and separation. In this work, we demonstrated that the separation performance can be optimized through tuning gate-opening pressure by temperature and realized the ternary mixture separation with a flexible framework NTU-65. Under optimized temperature, NTU-65 adsorbed large amount of C_2H_2 and CO_2 through gate-opening and only negligible amount of C_2H_4. Such selective adsorption enabled one-step separation of C_2H_4 from a ternary mixture of $C_2H_4/C_2H_2/CO_2$ and high purity C_2H_4 can be obtained through single breakthrough cycle. The ultralow C_2H_4 uptake also prevented its co-adsorption therefore yielded high percentage of recovered C_2H_4. Such gate-opening pressure optimization strategy would be broadly useful for separations by flexible MOFs. It is foreseeable that more multi-component separations will be realized by flexible MOFs in the near future.

Acknowledgements

We thank the financial support of the National Natural Science Foundation of China (21671102), the Young and Middle-aged Academic Leader of Jiangsu Provincial Blue Project, the Six Talent Peaks Project in Jiangsu Province (JY-030), the State Key Laboratory of Materials-Oriented Chemical Engineering (ZK201803) and award AX-1730 from Welch Foundation. The computational resources provided by the High Performance Computing Center of Nanjing Tech University is greatly appreciated.

Conflict of interest

The authors declare no conflict of interest.

Keywords: ethylene · gate-opening · metal–organic frameworks · separation · ternary mixtures

---

[1] a) R.-B. Lin, S. Xiang, W. Zhou, B. Chen, *Chem* **2020**, *6*, 337–363; b) P.-Q. Liao, N.-Y. Huang, W.-X. Zhang, J.-P. Zhang, X.-M. Chen, *Science* **2017**, *356*, 1193–1196; c) C. Gu, N. Hosono, J.-J. Zheng, Y. Sato, S. Kusaka, S. Sakaki, S. Kitagawa, *Science* **2019**, *363*, 387–391; d) L. Li, R.-B. Lin, R. Krishna, H. Li, S. Xiang, H. Wu, J. Li, W. Zhou, B. Chen, *Science* **2018**, *362*, 443–446; e) O. T. Qazvini, R. Babarao, Z.-L. Shi, Y.-B. Zhang, S. G. Telfer, *J. Am. Chem. Soc.* **2019**, *141*, 5014–5020; f) J. Duan, M. Higuchi, J. Zheng, S.-i. Noro, I. Y. Chang, K. Hyeon-Deuk, S. Mathew, S. Kusaka, E. Sivaniah, R. Matsuda, S. Sakaki, S. Kitagawa, *J. Am. Chem. Soc.* **2017**, *139*, 11576–11583; g) H. J. Yang, Y. X. Wang, R. Krishna, X. X. Jia, Y. Wang, A. N. Hong, C. Dang, H. E. Castillo, X. H. Bu, P. Y. Feng, *J. Am. Chem. Soc.* **2020**, *142*, 2222–2227; h) H. Li, L. Li, R.-B. Lin, W. Zhou, Z. Zhang, S. Xiang, B. Chen, *EnergyChem* **2019**, *1*, 100006; i) Q. Dong, Y. Guo, H. Cao, S. Wang, R. Matsuda, J. Duan, *ACS Appl. Mater. Inter.* **2020**, *12*, 3764.

[2] a) S. Krause, V. Bon, I. Senkovska, U. Stoeck, D. Wallacher, D. M. Tobbens, S. Zander, R. S. Pillai, G. Maurin, F.-X. Coudert, S. Kaskel, *Nature* **2016**, *532*, 348–352; b) M. Shivanna, Q.-Y. Yang, A. Bajpai, E. Patyk-Kazmierczak, M. J. Zaworotko, *Nat. Commun.* **2018**, *9*, 3080.

[3] R. Kitaura, K. Seki, G. Akiyama, S. Kitagawa, *Angew. Chem. Int. Ed.* **2003**, *42*, 428–431; *Angew. Chem.* **2003**, *115*, 444–447.

[4] S. Shimomura, M. Higuchi, R. Matsuda, K. Yoneda, Y. Hijikata, Y. Kubota, Y. Mita, J. Kim, M. Takata, S. Kitagawa, *Nat. Chem.* **2010**, *2*, 633–637.

[5] M. K. Taylor, T. Runčevski, J. Oktawiec, J. E. Bachman, R. L. Siegelman, H. Jiang, J. A. Mason, J. D. Tarver, J. R. Long, *J. Am. Chem. Soc.* **2018**, *140*, 10324–10331.

[6] a) R.-B. Lin, L. Li, H. Wu, H. Arman, B. Li, R.-G. Lin, W. Zhou, B. Chen, *J. Am. Chem. Soc.* **2017**, *139*, 8022–8028; b) T. Ke, Q. Wang, J. Shen, J. Zhou, Z. Bao, Q. Yang, Q. Ren, *Angew. Chem. Int. Ed.* **2020**, *59*, 12725–12730; *Angew. Chem.* **2020**, *132*, 12825–12830; c) J. Wang, Y. Zhang, P. Zhang, J. Hu, R.-B. Lin, Q. Deng, Z. Zeng, H. Xing, S. Deng, B. Chen, *J. Am. Chem. Soc.* **2020**, *142*, 9744–9751.

[7] Z. Bao, D. Xie, G. Chang, H. Wu, L. Li, W. Zhou, H. Wang, Z. Zhang, H. Xing, Q. Yang, M. J. Zaworotko, Q. Ren, B. Chen, *J. Am. Chem. Soc.* **2018**, *140*, 4596–4603.

[8] a) T.-L. Hu, H. Wang, B. Li, R. Krishna, H. Wu, W. Zhou, Y. Zhao, Y. Han, X. Wang, W. Zhu, Z. Yao, S. Xiang, B. Chen, *Nat. Commun.* **2015**, *6*, 7328; b) B. L. Farrell, V. O. Igenegbai, S. Linic, *ACS Catal.* **2016**, *6*, 4340–4346.

[9] K.-J. Chen, D. G. Madden, S. Mukherjee, T. Pham, K. A. Forrest, A. Kumar, B. Space, J. Kong, Q.-Y. Zhang, M. J. Zaworotko, *Science* **2019**, *366*, 241–246.

[10] a) X. Cui, K. Chen, H. Xing, Q. Yang, R. Krishna, Z. Bao, H. Wu, W. Zhou, X. Dong, Y. Han, B. Li, Q. Ren, M. J. Zaworotko, B. Chen, *Science* **2016**, *353*, 141–144; b) B. Li, X. Cui, D. O'Nolan, H.-M. Wen, M. Jiang, R. Krishna, H. Wu, R.-B. Lin, Y.-S. Chen, D. Yuan, H. Xing, W. Zhou, Q. Ren, G. Qian, M. J. Zaworotko, B. Chen, *Adv. Mater.* **2017**, *29*, 1704210.

[11] J.-R. Li, R. J. Kuppler, H. C. Zhou, *Chem. Soc. Rev.* **2009**, *38*, 1477–1504.

[12] a) A. O. Yazaydın, R. Q. Snurr, T. H. Park, K. Koh, J. Liu, M. D. Levan, A. I. Benin, P. Jakubczak, M. Lanuza, D. B. Galloway, J. J. Low, R. R. Willis, *J. Am. Chem. Soc.* **2009**, *131*, 18198–18199; b) J. E. Bachman, D. A. Reed, M. T. Kapelewski, G. Chachra, D. Jonnavittula, G. Radaelli, J. R. Long, *Energy Environ. Sci.* **2018**, *11*, 2423–2431.

[13] a) R.-B. Lin, L. Li, H.-L. Zhou, H. Wu, C. He, S. Li, R. Krishna, J. Li, W. Zhou, B. Chen, *Nat. Mater.* **2018**, *17*, 1128–1133; b) H. Wang, X. Dong, V. Colombo, Q. Wang, Y. Liu, W. Liu, X. L. Wang, X. Y. Huang, D. M. Proserpio, A. Sironi, Y. Han, J. Li, *Adv. Mater.* **2018**, *30*, 1805088; c) A. Cadiau, K. Adil, P. M. Bhatt, Y. Belmabkhout, M. Eddaoudi, *Science* **2016**, *353*, 137–140.

[14] H.-G. Hao, Y.-F. Zhao, D.-M. Chen, J.-M. Yu, K. Tan, S. Ma, Y. Chabal, Z.-M. Zhang, J.-M. Dou, Z.-H. Xiao, G. Day, H.-C. Zhou, T.-B. Lu, *Angew. Chem. Int. Ed.* **2018**, *57*, 16067–16071; *Angew. Chem.* **2018**, *130*, 16299–16303.

[15] H. Wang, X. Dong, E. Velasco, D. H. Olson, Y. Han, J. Li, *Energy Environ. Sci.* **2018**, *11*, 1226–1231.

[16] During our manuscript preparation, the crystal structure of the reported MOF was published: B.-Q. Song, Q.-Y. Yang, S.-Q. Wang, M. Vandichel, A. Kumar, C. Crowley, N. Kumar, C.-H. Deng, V. GasconPerez, M. Lusi, H. Wu, W. Zhou, M. J. Zaworotko, *J. Am. Chem. Soc.* **2020**, *142*, 6896–6901.

[17] S. Noro, R. Kitaura, M. Kondo, S. Kitagawa, T. Ishii, H. Matsuzaka, M. Yamashita, *J. Am. Chem. Soc.* **2002**, *124*, 2568 – 2583.

[18] S. Sen, N. Hosono, J.-J. Zheng, S. Kusaka, R. Matsuda, S. Sakaki, S. Kitagawa, *J. Am. Chem. Soc.* **2017**, *139*, 18313 – 18321.

[19] a) S. Bureekaew, H. Sato, R. Matsuda, Y. Kubota, R. Hirose, J. Kim, K. Kato, M. Takata, S. Kitagawa, *Angew. Chem. Int. Ed.* **2010**, *49*, 7660 – 7664; *Angew. Chem.* **2010**, *122*, 7826 – 7830; b) Y. Wang, Q. Dong, H. Cao, W. Ji, J. Duan, S. Jing, W. Jin, *Chem. Eur. J.* **2019**, *25*, 8790 – 8796.

[20] E. Nishibori, M. Takata, K. Kato, M. Sakata, Y. Kubota, S. Aoyagi, Y. Kuroiwa, M. Yamakata, N. Ikeda, *Nucl. Instrum. Methods Phys. Res. Sect. A* **2001**, *467 – 468*, 1045 – 1048.

[21] a) E. D. Bloch, W. L. Queen, R. Krishna, J. M. Zadrozny, C. M. Brown, J. R. Long, *Science* **2012**, *335*, 1606 – 1610; b) S. Yang, A. J. Ramirez-Cuesta, R. Newby, V. Garcia-Sakai, P. Manuel, S. K. Callear, S. I. Campbell, C.-C. Tang, M. Schroder, *Nat. Chem.* **2015**, *7*, 121 – 129.

[22] I. van Zandvoort, J. K. van der Waal, E.-J. Ras, R. de Graaf, R. Krishna, *Sep. Purif. Technol.* **2019**, *227*, 115730.

[23] P. Nugent, Y. Belmabkhout, S. D. Burd, A. J. Cairns, R. Luebke, K. Forrest, T. Pham, S. Ma, B. Space, L. Wojtas, M. Eddaoudi, M. J. Zaworotko, *Nature* **2013**, *495*, 80 – 84.

[24] H. Zeng, M. Xie, Y.-L. Huang, Y.-F. Zhao, X.-J. Xie, J.-P. Bai, M.-Y. Wan, R. Krishna, W.-G. Lu, D. Li, *Angew. Chem. Int. Ed.* **2019**, *58*, 8515 – 8519; *Angew. Chem.* **2019**, *131*, 8603 – 8607.

[25] A. T. Penteado, M. Kim, H. R. Godini, E. Esche, J.-U. Repke, *Front. Chem. Sci. Eng.* **2018**, *12*, 598 – 618.

[26] C. Gücüyener, J. van den Bergh, J. Gascon, F. Kapteijn, *J. Am. Chem. Soc.* **2010**, *132*, 17704 – 17706.

[27] Deposition Number 1961037 contains the supplementary crystallographic data for this paper. These data are provided free of charge by the joint Cambridge Crystallographic Data Centre and Fachinformationszentrum Karlsruhe Access Structures service www.ccdc.cam.ac.uk/structures.

Manuscript received: August 28, 2020
Accepted manuscript online: September 2, 2020
Version of record online: October 7, 2020

Angewandte Chemie
Eine Zeitschrift der Gesellschaft Deutscher Chemiker

Supporting Information

Tuning Gate-Opening of a Flexible Metal–Organic Framework for Ternary Gas Sieving Separation

Qiubing Dong[+], Xin Zhang[+], Shuang Liu[+], Rui-Biao Lin, Yanan Guo, Yunsheng Ma, Akira Yonezu, Rajamani Krishna, Gongpin Liu, Jingui Duan, Ryotaro Matsuda, Wanqin Jin, and Banglin Chen**

anie_202011802_sm_miscellaneous_information.pdf

General Procedures and Materials

All reagents and solvents were commercially available and used as received. The elemental analysis was carried out with a Perkin-Elmer 240C elemental analyzer. The Fourier-transform Infrared (FT-IR) spectra were recorded from KBr pellets in the range of 4000–600 cm^{-1} on a VECTOR 22 spectrometer. Thermogravimetric analyses (TGA) were performed using a STA 209 F1 (NETZSCH Instruments) thermo-microbalance, heating from room temperature to 650°C at a rate of 10°C min^{-1} under nitrogen flow. ^{1}H NMR spectra were recorded on a Bruker Advance III 600 MHz NMR Spectrometer. Simulated powder patterns from single-crystal X-ray diffraction data were generated using Mercury 1.4.2 software. Powder synchrotron X-ray diffraction patterns were collected at SPring-8 BL02B2 beamline. The coincident PXRD/adsorption measurements were performed with a Rigaku SmartLab with CuKα radiation connected to a BELSORP-18PLUS volumetric adsorption setup (MicrotracBEL Japan, Inc.) equipped with a custom-made cryostat apparatus. The respective apparatuses were synchronized to enable each PXRD pattern to be obtained at each equilibrium point of the sorption isotherms. Activated carbon (NORIT SX 1, S_{BET}~1100 m^2/g) was purchased from NORIT.

Ligand synthesis

Synthesis of 1,4-di(1H-imidazol-1-yl)benzene (**L^1**): A mixture of 1,4-dibromobenzene (1.17 g, 5 mmol), imidazole (1.43 g, 21 mmol), K_2CO_3 (2.18 g, 15.75 mmol) and $CuSO_4$ (16 mg, 0.1 mmol) were charged into a Teflon-lined autoclave (50 mL) under N_2 atmosphere and heated to 180 ^oC and kept for 24 h. After the temperature cooling down, the crude product was washed with water for three times. The solid residue was then extracted with dichloromethane, upon removal of the solvent at 50 ^oC. **L^1** as a pale-yellow solid was obtained (Yield: 85%). ^{1}H NMR (400 MHz, $CDCl_3$): *d* = 7.254 (s, 2H), 7.320 (s, 2H), 7.536 (s, 4H), 7.895 (s, 2H).

Synthesis of NTU-65 crystal.

1 mL of **L1** (0.11 g, 0.50 mmol) solution in *N*,*N'*-dimethylformamide (DMF) was slowly layered on aqueous solution (0.5 mL) of $CuSiF_6 \cdot 6H_2O$ (4 mg, 0.014 mmol), where the middle layer is DMF/MeOH/H_2O (3/3/0.5, 1.5 mL). After a week purple single-crystals of **NTU-65** was obtained with high yield (40%, based on **L1**).

Single crystal X-ray studies

Single-crystal X-ray diffraction measurements were performed on a Bruker Smart Apex CCD diffractometer at 298 K using graphite monochromator Mo/Kα radiation (λ = 0.71073 Å). Data reduction was made with the Bruker Saint program. The structures were solved by direct methods and refined with full-matrix least squares technique using the SHELXTL package[1]. Non-hydrogen atoms were refined with anisotropic displacement parameters during the final cycles. Organic hydrogen atoms were placed in calculated positions with isotropic displacement parameters set to 1.2 × Ueq of the attached atom. The unit cell includes disordered solvent molecules, which could not be modeled as discrete atomic sites. We employed PLATON/SQUEEZE[2-3] to calculate the diffraction contribution of the solvent molecules and, thereby, to produce a set of solvent-free diffraction intensities; structures were then refined again using the data generated. CCDC 1961037 contains the supplementary crystallographic data for this paper. These data can be obtained free of charge from The Cambridge Crystallographic Data Centre via www.ccdc.cam.ac.uk/data_request/cif. Crystal data are summarized in Table S1.

Table S1. Crystal information of NTU-65

	NTU-65
Empirical formula	$C_{24}H_{20}CuF_6N_8Si$
Formula weight	626.12
Crystal system	*monoclinic*
Space group	$P2_1/c$
Unit cell dimensions (Å)	a =13.223(3)
	b =25.430(5)
	c =12.625(2)
	β =117.557(4)
Volume (Å^3)	3763.7(13)
Z	4
Density (calculated) (g/cm^3)	1.105
Mu (MoKa) (mm^{-1})	0.664
$F_{(000)}$	1268
Theta min-max	2.0, 25.1
Index ranges	-14<=h<=15
	-30<=k<=27
	-15<=l<=15
Tot , Uniq Data, R(int)	21224, 6611, 0.065
Observed data [I > 2σ (I)]	4798
Nref, Npar	6611, 361
R_1, wR_2, S	0.1037, 0.2634, 1.07
Max Shift	0

$R = \Sigma||F_o|-|F_c||/\Sigma|F_o|$, $wR = \{\Sigma[w(|F_o|^2 - |F_c|^2)^2]/\Sigma[w(|F_o|^4)]\}.^{1/2}$ and $w = 1/[\sigma^2(F_o^2) + (0.1452P)^2]$ where $P = (F_o^2+2F_c^2)/3$

Structure view of NTU-65

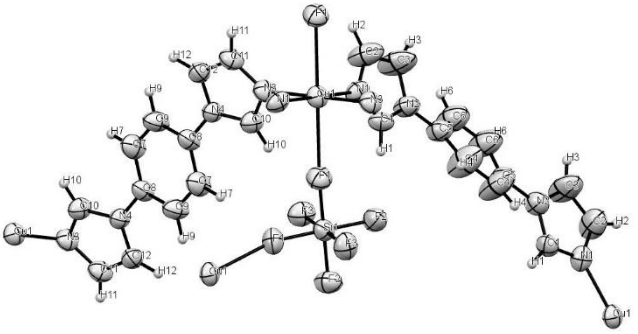

Figure S1. View of the coordination environments of NTU-65.

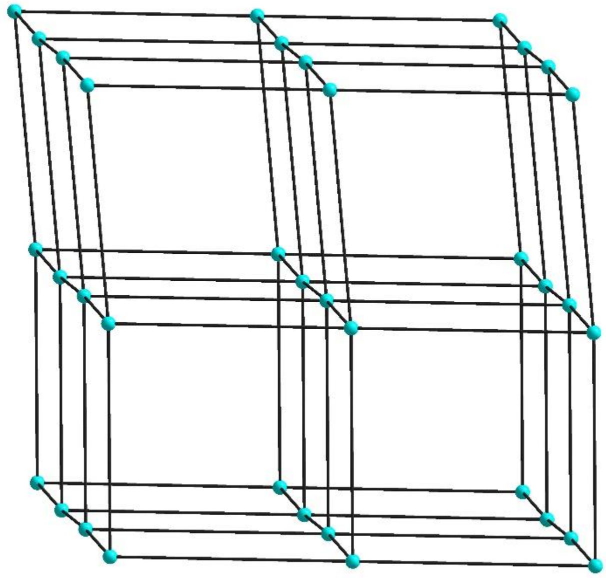

Figure S2. The simplified **pcu** topology of NTU-65.

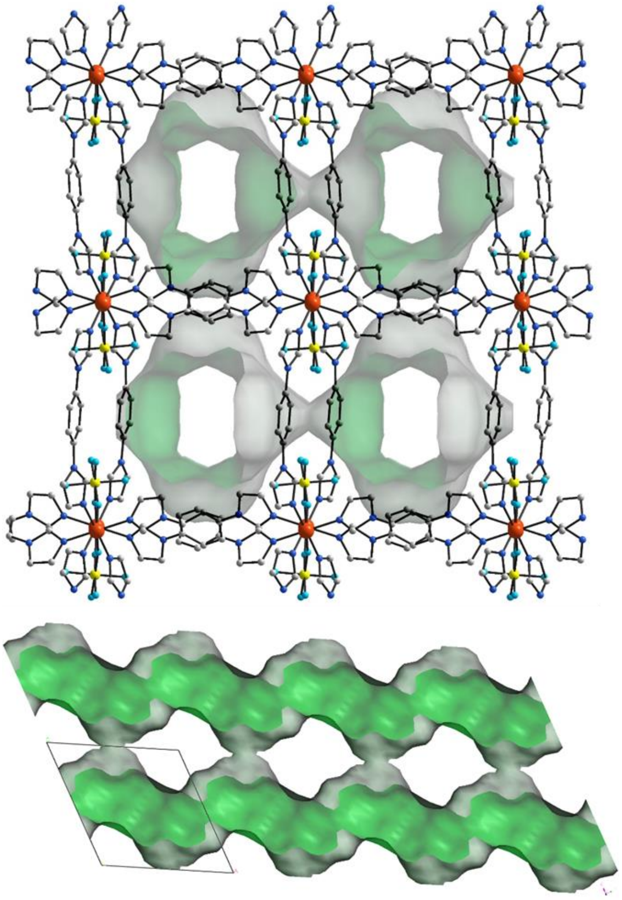

Figure S3. Packing view of NTU-65 framework along *a*-axis (above) and the accessible nanopore space (below), highlighted by green color.

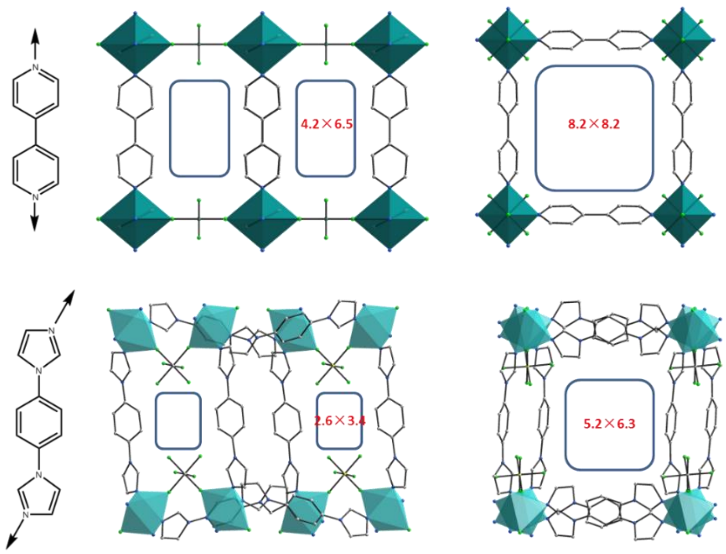

Figure S4. Structure comparison of SIFSIX-Cu (above) and **NTU-65** (below), where the unit of the parameters is Å.

Table S2. Hydrogen bond geometry (Å, °) of NTU-65.

D - H…A					*D* - H	H…A	*D*…A	*D* - H…A
C3	--	H3	…	F1	0.930	2.535	3.069(11)	116.76
C15	--	H15	…	F1	0.930	2.545	3.099(10)	118.62
C3	--	H3	…	F2	0.930	2.366	3.285(10)	169.55
C10	--	H10	…	F3	0.930	2.629	3.159(10)	116.75
C18	--	H18	…	F4	0.930	2.483	3.389(13)	164.21
C24	--	H24	…	F4	0.930	2.136	2.968(11)	148.40
C10	--	H10	…	F5	0.930	2.247	3.166(10)	169.52
C6	--	H6	…	F5	0.930	2.583	3.499(11)	168.23
C15	--	H15	…	F6	0.930	2.137	3.066(10)	179.12
C17	--	H17	…	F6	0.930	2.441	3.343(12)	163.20

Basic characterization

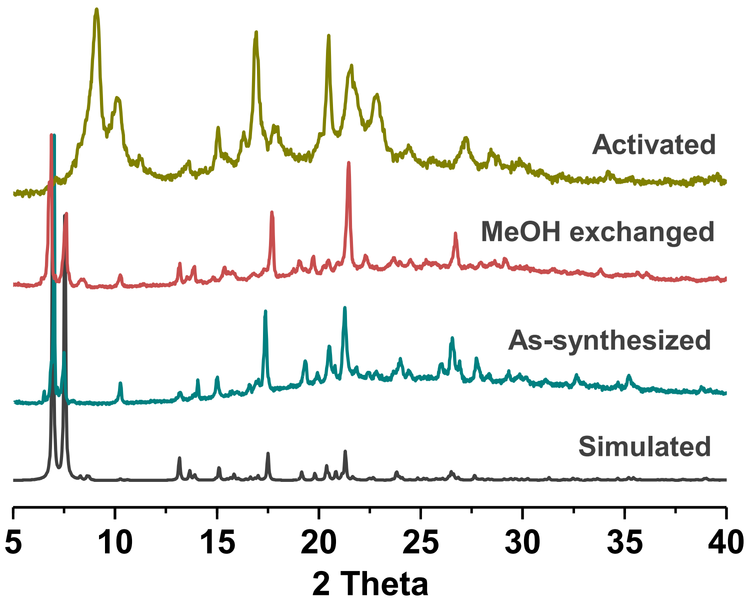

Figure S5. PXRD patterns of NTU-65.

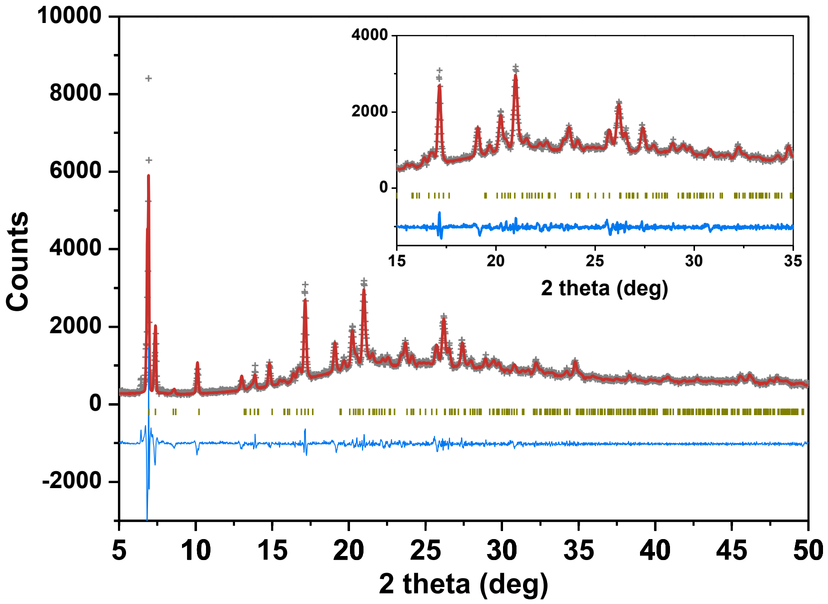

Figure S6. The results of LeiBail analysis for the PXRD of as-synthesized NTU-65. The experimental data are presented as grey plots, the calculated data by red line and difference as blue line. Refined parameters and reliability factors are as follows: a = 12.4275 Å; b = 24.7912 Å; c = 13.0863 Å; β = 117.4232°; R_p: 0.0472 and R_{wp}: 0.0944.

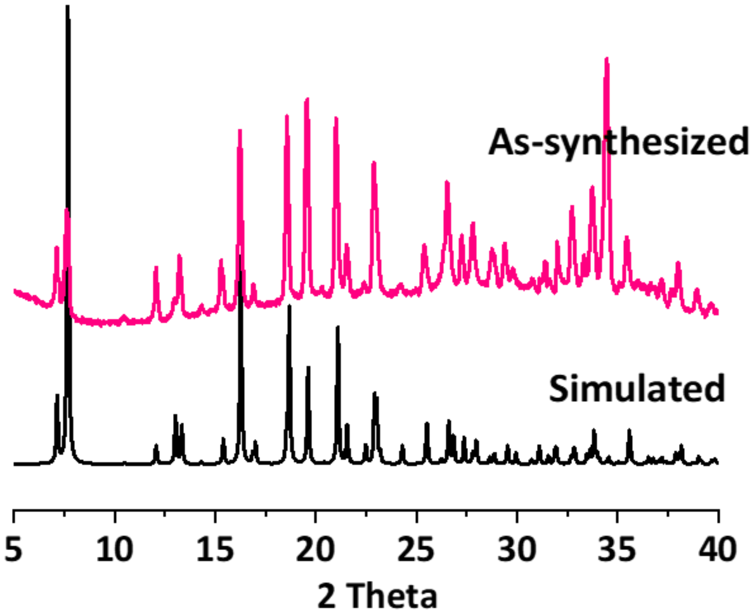

Figure S7. PXRD patterns of ZIF-7.

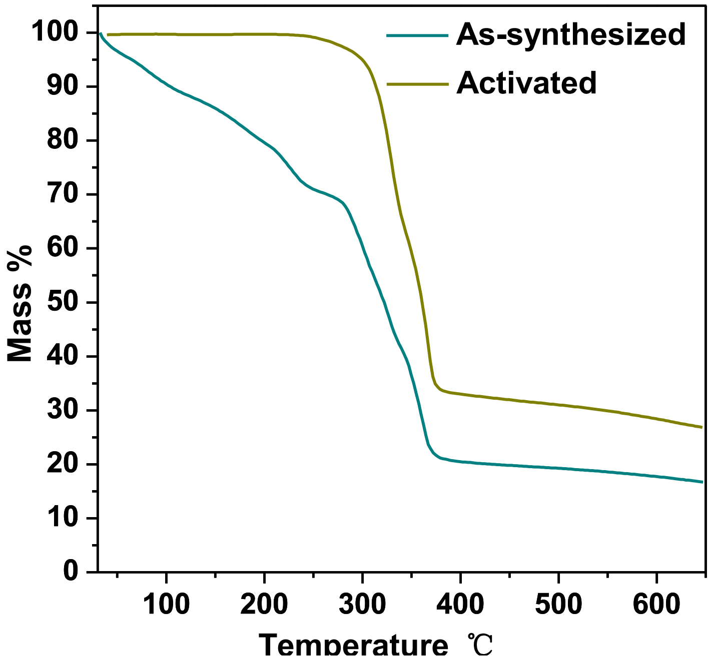

Figure S8. TG curves of NTU-65.

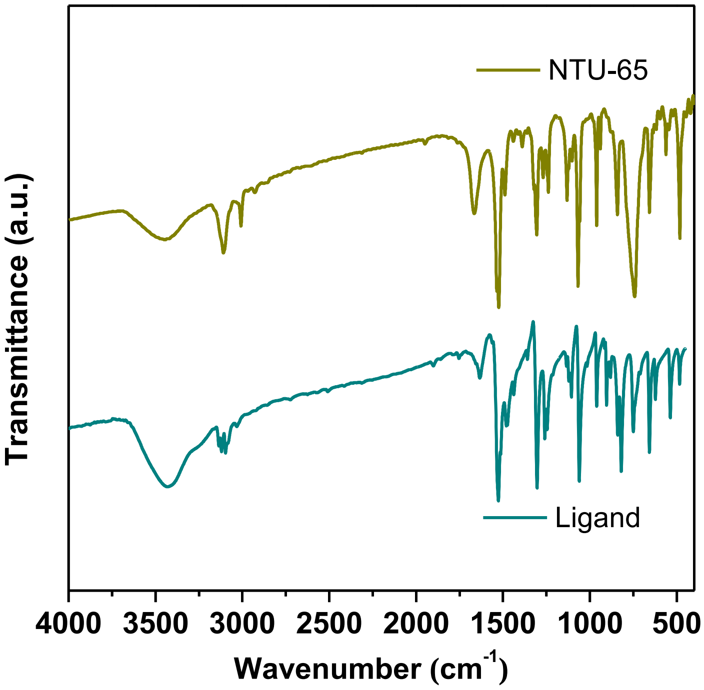

Figure S9. Infrared spectra of L1 ligand and NTU-65.

Activation of crystal NTU-65

Solvent-exchanged crystal was prepared by immersing the as-synthesized samples in dry MeOH for two days to remove the nonvolatile solvents, and the extract was decanted every 8 h and fresh MeOH was replaced. The completely activated sample was obtained by heating the solvent-exchanged sample at 25°C for 6 h, 60°C for 6 h and then 120°C for 20 h under a dynamic high vacuum.

Single gas adsorption measurements.

In the gas sorption measurement, ultra-high-purity grade were used throughout the adsorption experiments. N_2 sorption isotherm has been repeated twice to confirm the reproducibility within experimental error. Gas adsorption isotherms were obtained using a Belsorpvolumetric adsorption instrument (BEL Japan Corp.).

Selectivity Prediction for Binary Mixture Adsorption

Ideal adsorbed solution theory (IAST) was used to predict binary mixture adsorption from the experimental pure-gas isotherms. To perform the integrations required by IAST, the single-component isotherms should be fitted by a proper model. There is no restriction on the choice of the model to fit the adsorption isotherm, however, data over the pressure range under study should be fitted very precisely.

The unary isotherm data for C_2H_2, C_2H_4, and CO_2 in NTU-65 were measured at 273 K, 283 K, 298 K, 313 K, and 333 K. The C_2H_2 isotherms were fitted with the dual-site Langmuir-Freundlich model. The CO_2 isotherm at 263 K was fitted with the dual-site Langmuir-Freundlich model; for higher temperatures of 283 K, and 298 K. The unary CO_2 isotherms were fitted with the 1-site Langmuir model.

$$q = q_{A,sat}\frac{b_A p^{\nu A}}{1+b_A p^{\nu A}} + q_{B,sat}\frac{b_B p^{\nu B}}{1+b_B p^{\nu B}} \qquad (1)$$

The C_2H_4 isotherms were fitted with the 1-site Langmuir model

$$q = q_{sat}\frac{bp}{1+bp} \qquad (2)$$

The C_2H_2, C_2H_4 and CO_2 fit parameters are provided in Table S3-5, respectively.

The adsorption selectivity for binary mixture

$$S_{ads} = \frac{q_1/q_2}{p_1/p_2} \qquad (3)$$

The separation performance in fixed bed adsorbers is dictated not only by selectivity, but also the uptake capacity. For this reason, a combined metric, called the separation potential, was introduced recently by Krishna.[6, 7] This combined metric Δq, represents the maximum number of moles of pure component 2 (the less strongly adsdorbed species, C_2H_4 in this case) that can be recovered in the gas phase per kg of adsorbent in the fixed bed.

$$\Delta q = \left(q_1 \frac{y_2}{y_1} - q_2 \right) \qquad (4)$$

where q_1, q_2 are the molar loadings (units: mol kg^{-1}) for mixture adsorption, calculated from the IAST.

Breakthrough simulations

The performance of industrial fixed bed adsorbers is dictated by a combination of adsorption selectivity and uptake capacity. Transient breakthrough simulations were carried out for various binary and ternary mixtures, using the methodology described in earlier publications.[4-7] For the breakthrough simulations, the following parameter values were used: length of packed bed, L = 0.3 m; voidage of packed bed, ε = 0.4; superficial gas velocity at inlet, u = 0.04 m/s. The *y*-axis is the dimensionless concentrations of each component at the exit of the fixed bed, normalized with respect to the inlet feed concentrations. The *x*-axis is the *dimensionless* time, $\tau = \frac{tu}{L\varepsilon}$, defined by dividing the actual time, *t*, by the characteristic time, $\frac{L\varepsilon}{u}$.

Notation of the section of IAST and breakthrough simulation: b is Langmuir-Freundlich constant, $\mathrm{Pa}^{-\nu}$; q is component molar loading of species i, mol kg^{-1}; q_{sat} is saturation loading, mol kg^{-1}; L is length of packed bed adsorber, m; t is time, s; T is absolute temperature, K; u is superficial gas velocity in packed bed, m s^{-1}; Greek letters of ε is voidage of packed bed, dimensionless; ν is Freundlich exponent, dimensionless and τ is time, dimensionless.

Breakthrough measurements

The automatic equipment used in this study is designed and hand-made by our group member according to the literatures [8-10]. The flow rates of all gases are regulated by mass flow controllers (Acceptable range for each 0-20 mL), and the effluent gas stream from the column is monitored by gas chromatography (GC) detector. All measurements were performed following a protocol established by literatures[8-10]. The initial activated **NTU-65** crystals (1.2 g) were packed into a stainless-steel column tightly. Then, the column was firstly activated by dynamic vacuum under 120°C. swept with He flow under 120°C until no other gases were detected in the effluent. Then, a mixture flow was dosed into the column. Breakpoints were determined when the first peak was detected. For the cycling of breakthrough experiments, the sample was regenerated by desorption under He flow for 20 min at 358 K.

Figure S10. View of the automatic breakthrough equipment designed and used in our group.

Porosity and adsorption of NTU-65

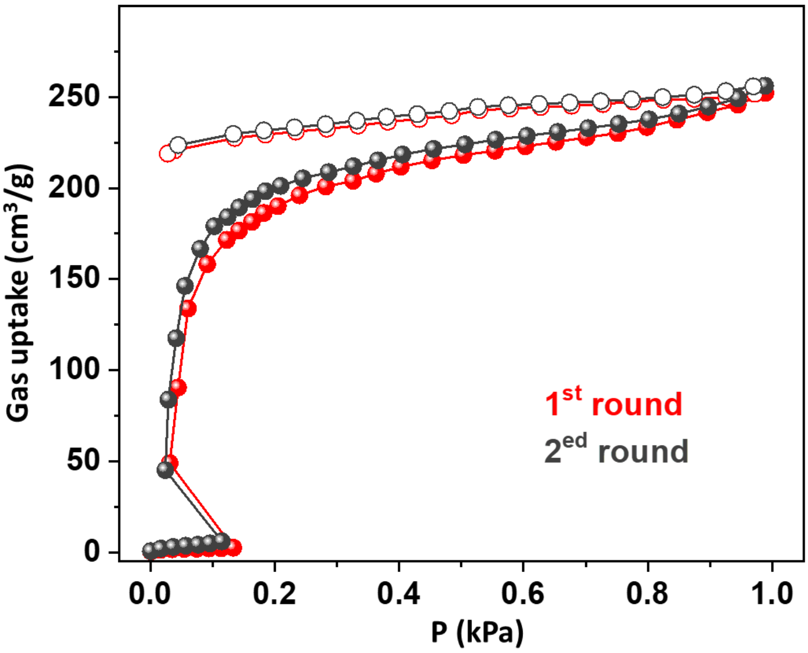

Figure S11. Two rounds of N_2 adsorption by NTU-65 at 77 K.

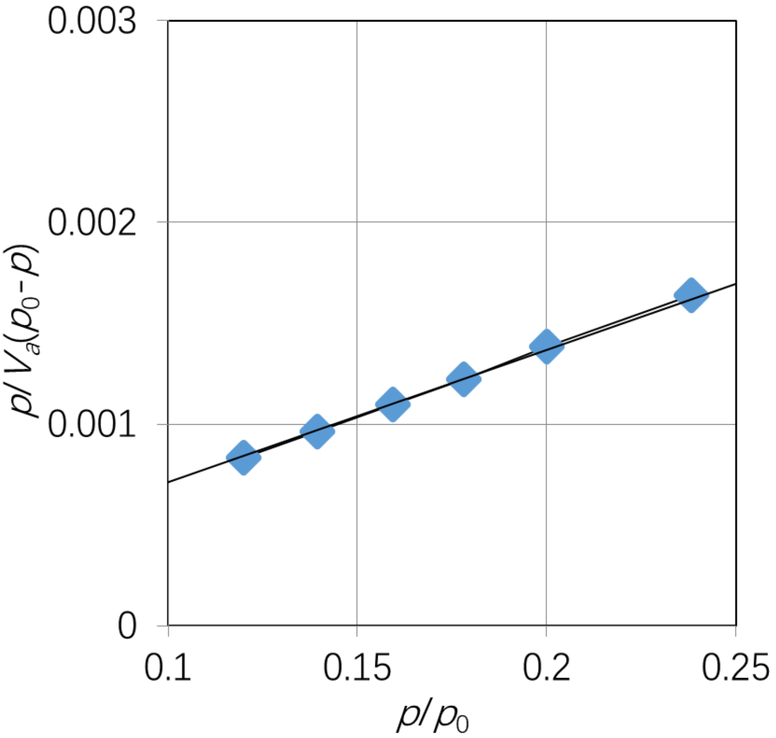

Figure S12. The consistency plot for BET fitting in NTU-65.

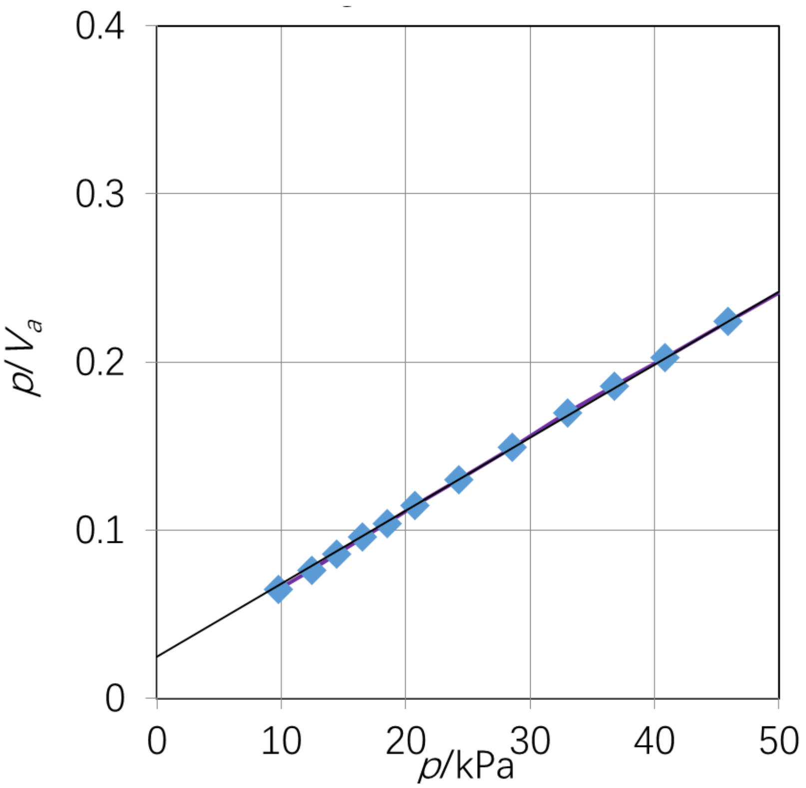

Figure S13. The consistency plot for Langmuir fitting in NTU-65.

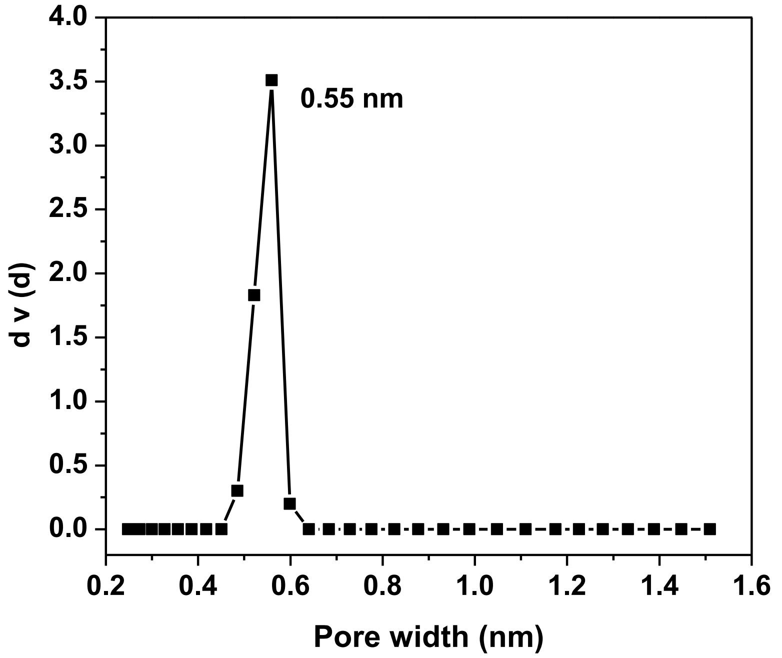

Figure S14. Pore size of NTU-65 determined by N_2 adsorption at 77 K.

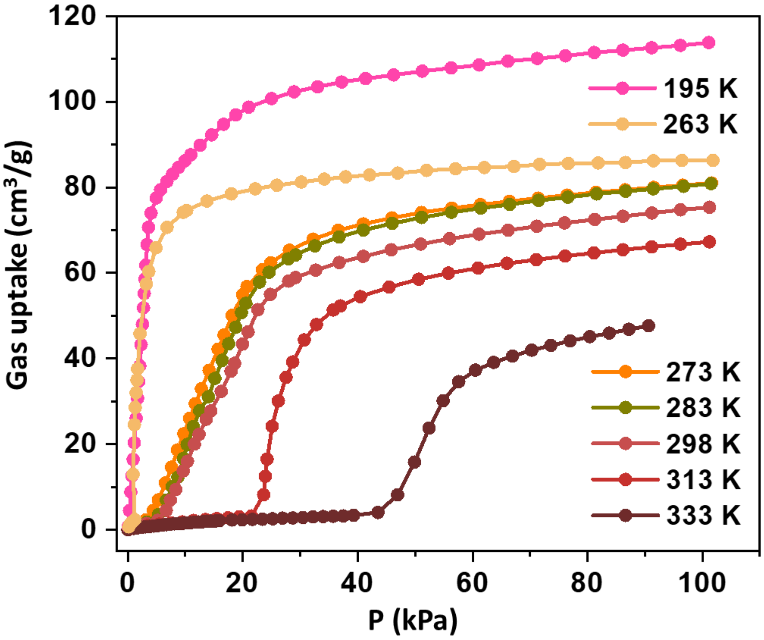

Figure S15. C_2H_2 adsorption of NTU-65 at different temperatures.

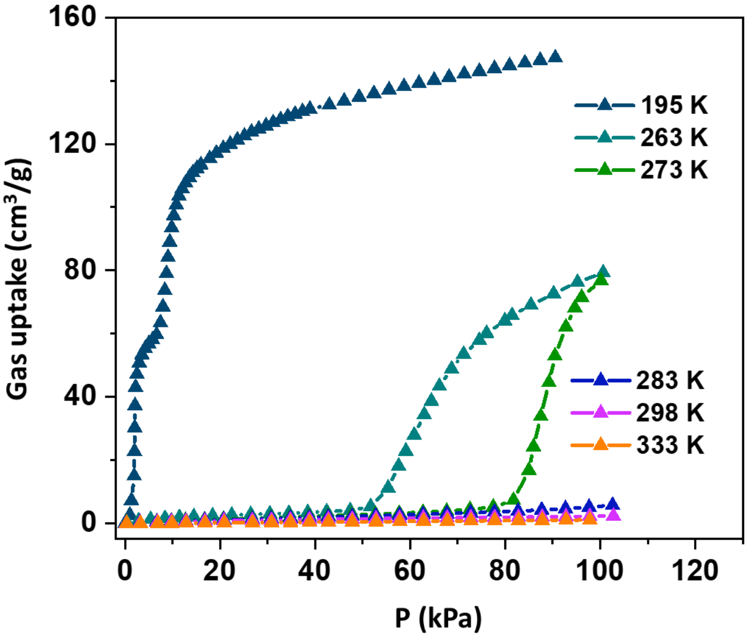

Figure S16. CO_2 adsorption of NTU-65 at different temperatures.

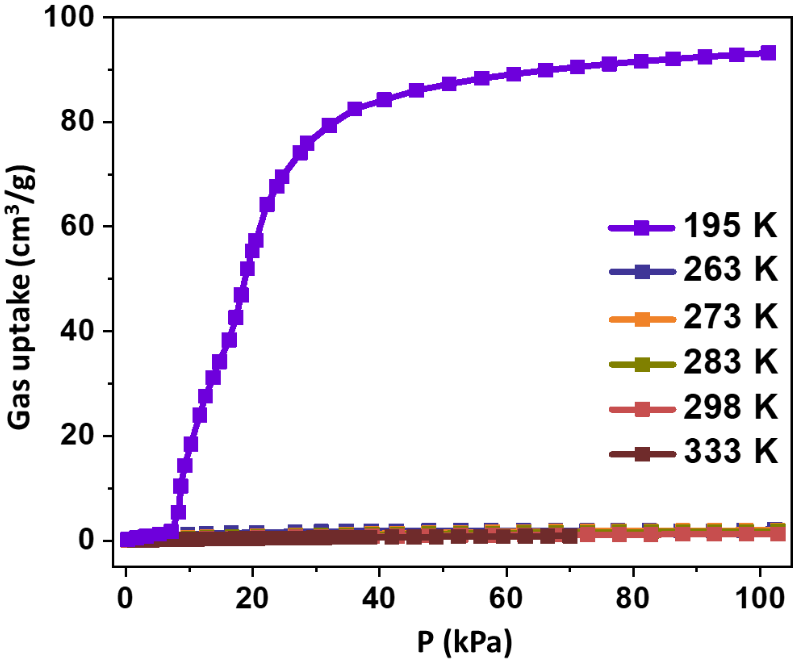

Figure S17. C_2H_4 adsorption of NTU-65 at different temperatures.

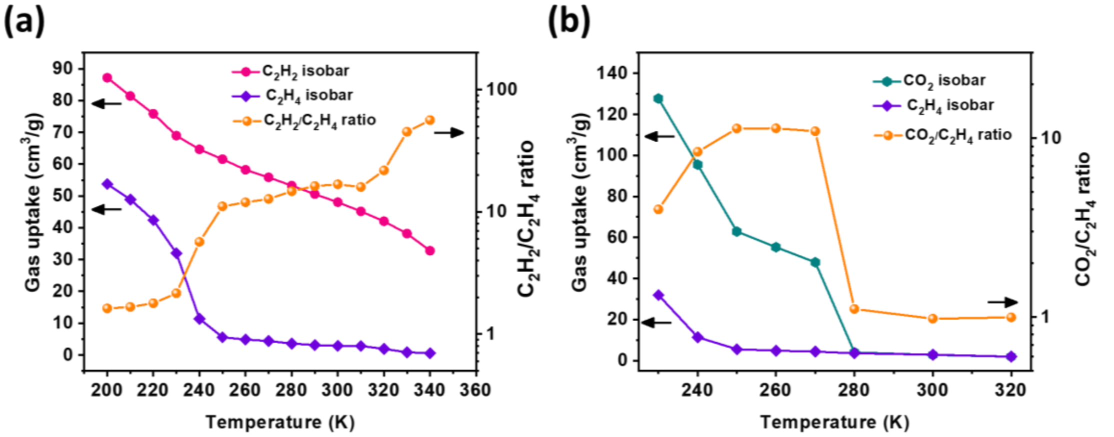

Figure S18. Adsorption isobars and uptake ratios of NTU-65. (a) Adsorption isobars of C_2H_2 (pink) and C_2H_4 (purple), uptake ratio C_2H_2/C_2H_4 (orange); (b) Adsorption isobars of CO_2 (cyan) and C_2H_4 (purple), uptake ratio CO_2/C_2H_4 (orange).

Calculation details

In order to get a comprehensive understanding of the interaction properties of C_2H_2 with NTU pore surfaces, a cluster model including eight ligands were cut from the crystal structure (see Figure S13). The structural model covers the two types of pores existing in NTU crystal. All calculations were performed through the Vienna Ab-initio Simulation Package (VASP).[11] The Dudarev's approach[12] was used for the GGA+U calculations, in which the on site Coulomb interaction for the localized Cu *d* orbitals was parametrized by $U_{\mathrm{eff}} = U - J$. The optimal U_{eff} of 4.0 eV for Cu was taken from ref. [13] All eight Cu atoms were fixed throughout the computations. The long-range dispersion effect was included through the Grimme's semi-empirical correction for the dispersion potential (DFT-D3).[14] The projector augmented wavefunction (PAW)[15] method was employed to describe the electron-core interactions. The Perdew-Burke-Ernzerhof (PBE) functional in a plane wave pseudopotential implementation within the generalized gradient approximation (GGA) was used to detail with the electron exchange-correlation.[16] The plane wave cutoff energies of 450 eV were adopted for the cluster models. Since the cluster was put in the centre of a big vacuum box (52 Å × 52 Å × 52 Å), the 1×1×1 Monkhorst-Pack mesh sampling *k*-points in the Brillouin zone was employed.[17] The Gaussian smearing with the width of 0.1 eV was applied. The electronic self-consistent iteration convergence criterion was set to be 1.0×10^{-5} eV, and the convergence tolerance of force acting on each free atom was 0.05 eV/Å.

The binding energy per C_2H_2 was calculated through equation (1):

$$\Delta E = (E_{\mathrm{NTU}} + n\cdot E_{\mathrm{C2H2}} - E_{\mathrm{NTU+C2H2}})/n \qquad (1)$$

where E_{NTU}, E_{C2H2} and $E_{\mathrm{NTU+C2H2}}$ are the energy of isolated NTU cluster, the energy of isolated C_2H_2 molecule, and the energy of NTU cluster binding with *n* C_2H_2 molecules, respectively. A postive ΔE_{bind} means that the corresponding binding of C_2H_2 is exothermic. The larger of ΔE_{bind}, the stronger of the adsorption and the more stable of the binding system.

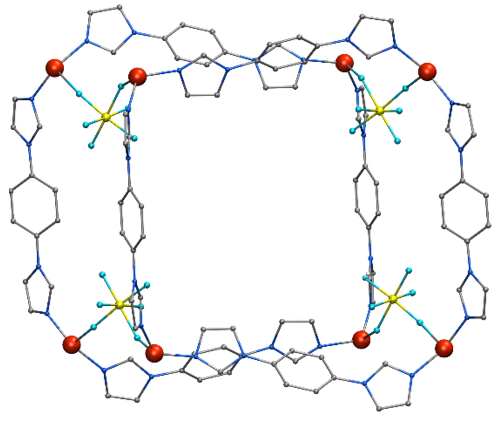

Figure S19. The geometrically optimized cluster model of NTU-65. H atoms are not shown. The color codes for atoms are as follows: C, grey; H, white; N, blue; F, cyan; Si, yellow; Cu, red.

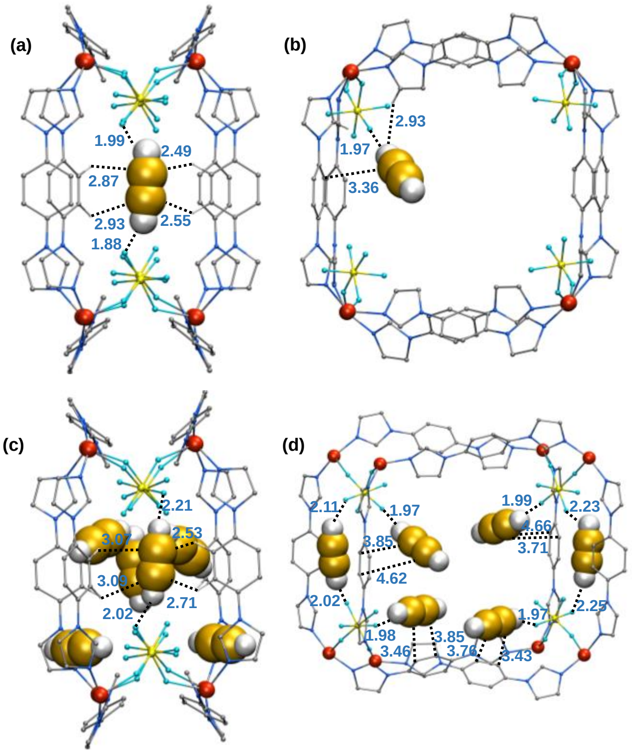

Figure S20. DFT calculation: view of the optimized structures of (a) *conf_1*, (b) *conf_2*, and (c-d) NTU-65-6C_2H_2 in two directions. The closest contacts between NTU atoms and C_2H_2 C/H atoms are shown in Å. C_2H_2 molecules are displayed in space-filling mode. The colour codes for atoms are as follows: C, grey; H, white; N, blue; F, cyan; Si, yellow; Cu, red.

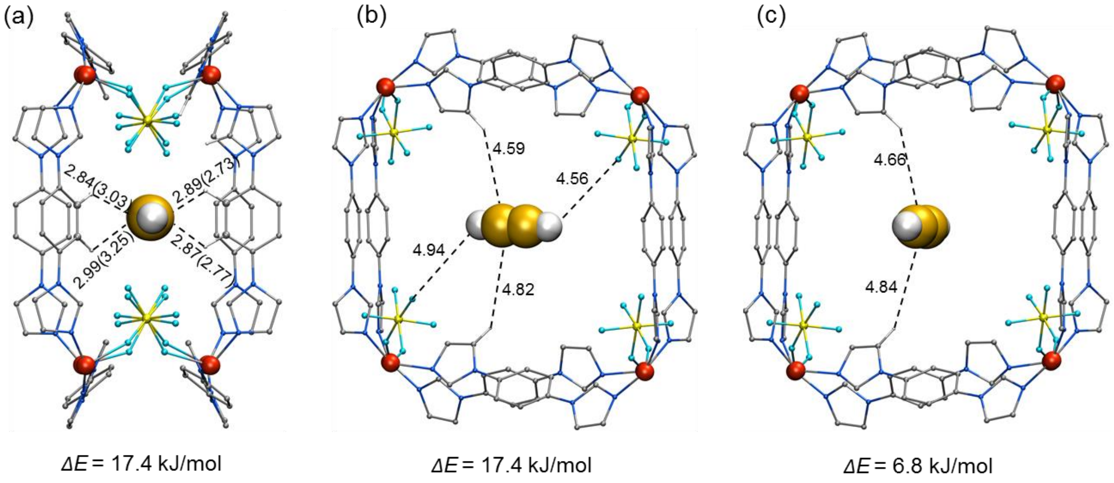

Figure S21. The optimized configurations (*conf_3* to *_5*) of C_2H_2 on NTU-65. The closest contacts between NTU-65 atoms and C/H atoms of C_2H_2 are shown in Å. In (a), the values in the parentheses denote the distances between the $\mathbf{H_{NTU\text{-}65}}$ atoms and the $\mathbf{C_{C2H2}}$ atoms far from the view. The binding energies are listed below at the bottom of each subfigure. Only H atoms contacting with C_2H_2 were shown. C_2H_2 molecules are displayed in space filling mode. The color codes for atoms are as follows: C, grey; H, white; N, blue; F, cyan; Si, yellow; Cu, red.

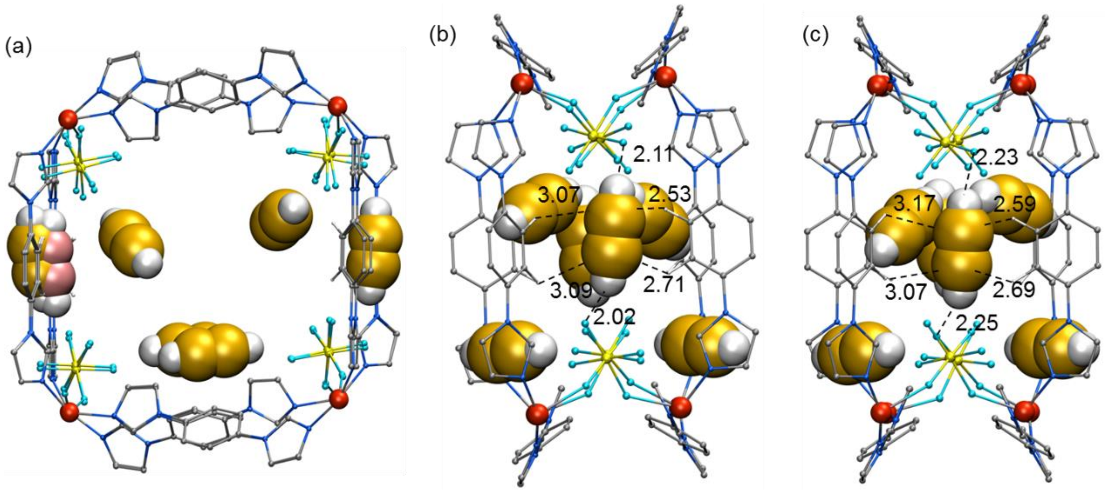

Figure S22. The superposition of the NTU-65-6C_2H_2 and the *conf_1* model. In the *conf_1* model, the C_2H_2 molecule (pink) lies almost in the plane formed by two side aromatic rings. Relatively, in the NTU-65-6C_2H_2 model, the C_2H_2 molecules are out of the plane. (b, c) The views of the two C_2H_2 molecules trapped by two SiF_6^{2-} anions and two ligands of NTU-65 in the NTU-65-6C_2H_2 model. The nearest atomic distances are shown in Å. C_2H_2 molecules are displayed in space filling mode and the carbon atoms of C_2H_2 molecule in *conf_1* model are in pick. The color codes for other atoms are as follows: C, grey; H, white; N, blue; F, cyan; Si, yellow; Cu, red.

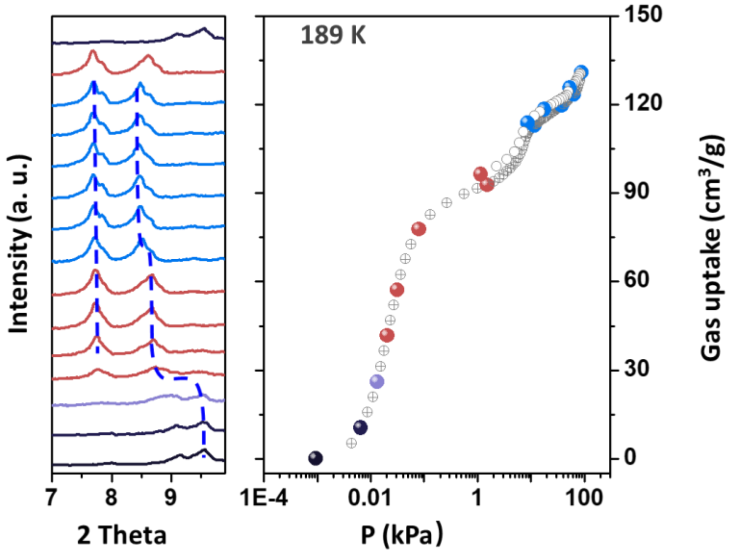

Figure S23. *In situ* coincident PXRD/adsorption of C_2H_2 in **NTU-65** at 189 K.

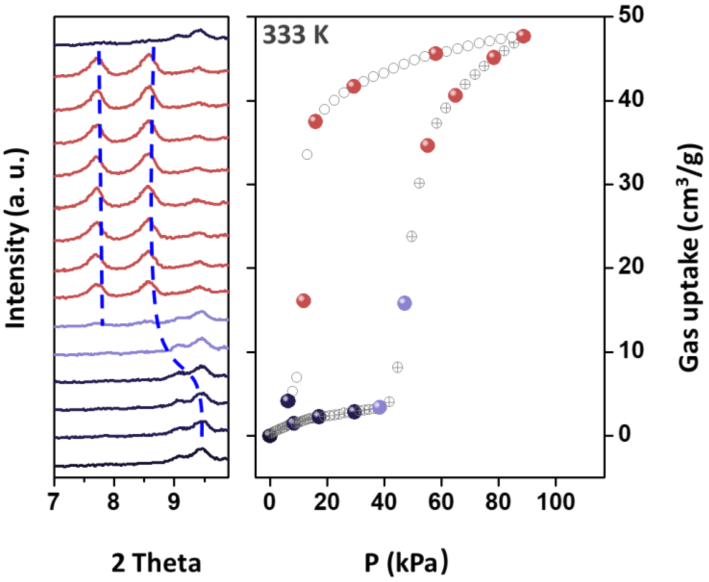

Figure S24. *In situ* coincident PXRD/adsorption of C_2H_2 in **NTU-65** at 333 K.

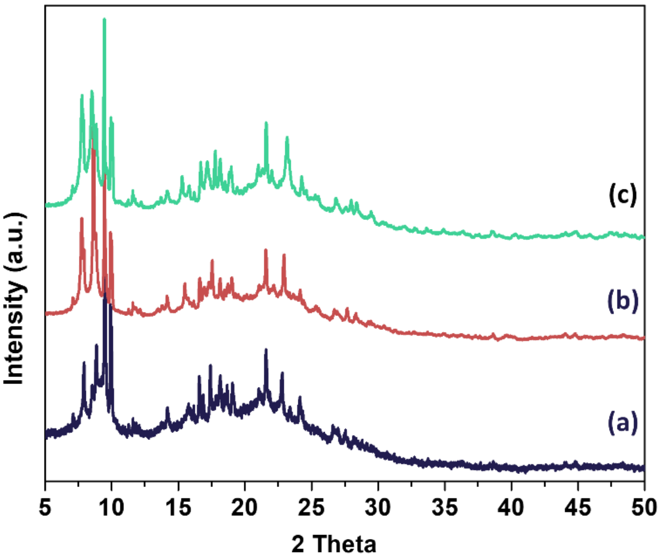

Figure S25. The powder synchrotron X-ray diffraction patterns of **NTU-65:** fully activated **NTU-65** (a), C_2H_2 absorbed at 333 K (1 bar) (b), and C_2H_2 absorbed at 189 K (c).

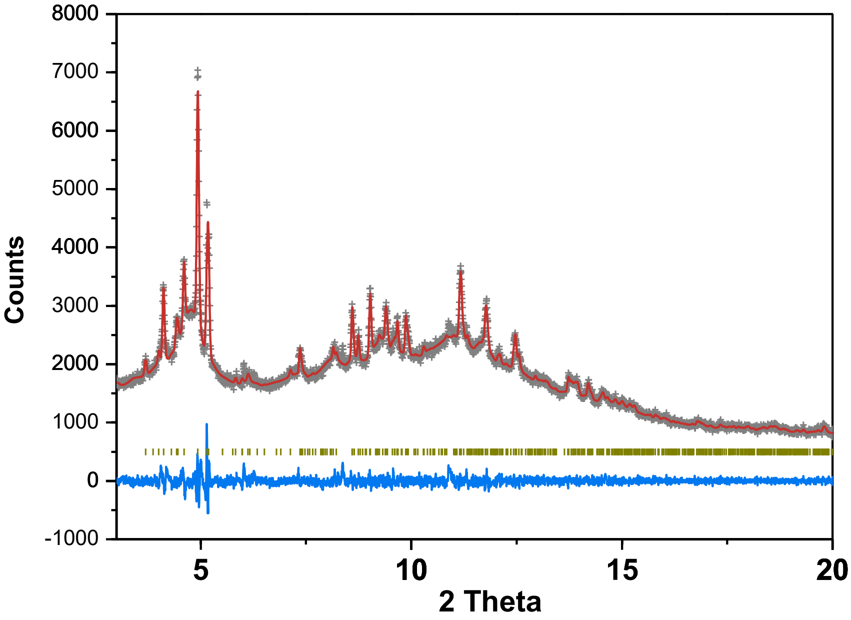

Figure S26. The results of LeiBail analysis for the synchrotron PXRD of fully activated **NTU-65**. The experimental data are presented as grey plots, the calculated data by red line and difference as blue line. Refined parameters and reliability factors are shown in Table S3.

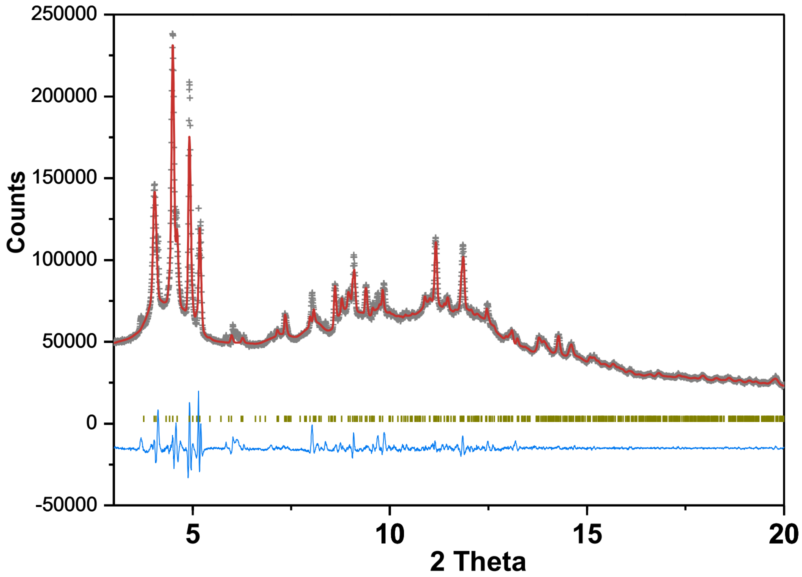

Figure S27. The results of LeiBail analysis for the synchrotron PXRD of **NTU-65** with absorbed C_2H_2 at 333 K (1 bar). The experimental data are presented as grey plots, the calculated data by red line and difference as blue line. Refined parameters and reliability factors are shown in Table S3.

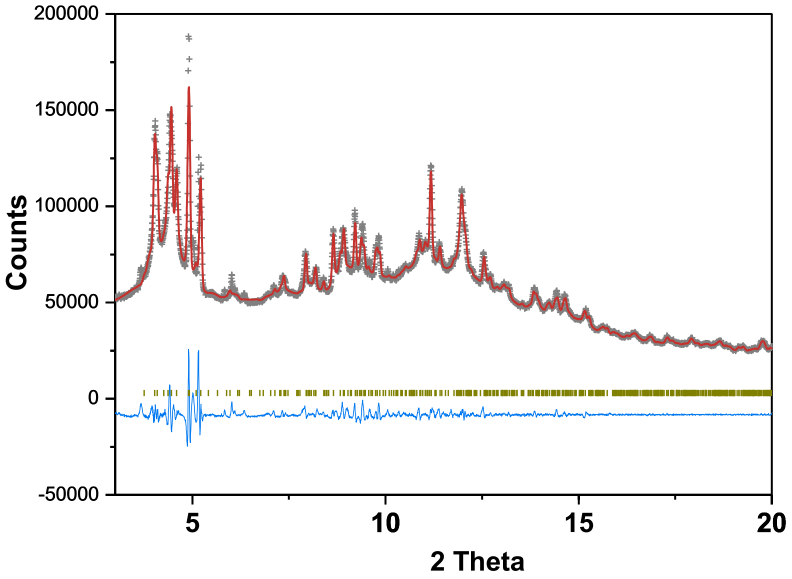

Figure S28. The results of LeiBail analysis for the synchrotron PXRD of **NTU-65** with absorbed C_2H_2 at 189 K (1 bar). The experimental data are presented as grey plots, the calculated data by red line and difference as blue line. Refined parameters and reliability factors are shown in Table S3.

Table S3. Refined parameters and reliability factors of the synchrotron PXRD of **NTU-65**.

	fully activated	C_2H_2 absorbed at 333 K (1 bar)	C_2H_2 absorbed at 189 K
a (Å)	22.4815	23.2138	23.2832
b (Å)	12.9785	13.1841	13.2319
c (Å)	12.2891	11.4516	11.6310
α (˚)	104.678	110.074	109.518
β (˚)	90.8039	96.6335	96.4013
γ (˚)	96.3472	93.1245	92.2609
V (Å^3)	3444.07	3253.15	3345.07
R_p	0.02503	0.02523	0.02478
R_{wp}	0.03346	0.04235	0.04338

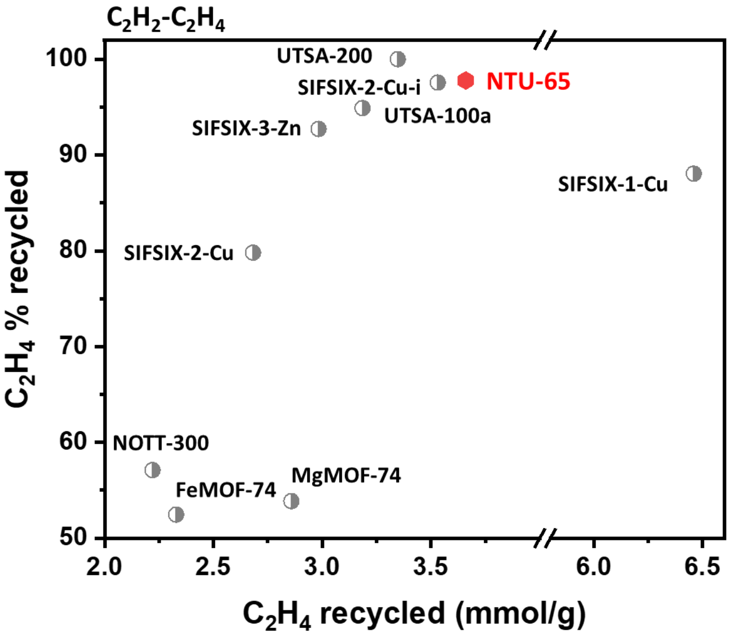

Figure S29. C_2H_2/C_2H_4 separation performance. Amount and percentage of C_2H_4 recovered from C_2H_2/C_2H_4 (50/50, v/v) by NTU-65 in comparison with benchmark materials.

Table S4. Dual-site Langmuir-Freundlich parameter fits for C_2H_2 in NTU-65 at various temperatures *T*.

T K	$q_{A,sat}$ mol kg^{-1}	b_A $Pa^{-\nu A}$	A dimensionless	$q_{B,sat}$ mol kg^{-1}	b_B $Pa^{-\nu B}$	B dimensionless
273	4.8	6.332E-05	0.67	3	6.605E-12	2.7
283	4.8	5.521E-05	0.67	3	4.625E-12	2.7
298	3	6.175E-05	0.7	2.8	3.113E-14	3.2
313	0.2	4.264E-04	0.8	2.55	4.524E-57	12.7
333	0.2	5.283E-05	1	1.8	5.377E-65	13.6

Table S5. 1-site Langmuir parameter fits for C_2H_4 in NTU-65 at various temperatures *T*.

T K	$q_{A,sat}$ mol kg^{-1}	b_A Pa^{-1}
263	0.096	1.3E-05
273	0.126	2.318E-05
283	0.114	2.120E-05
298	0.082	2.139E-05
333	0.064	1.966E-05

Table S6. Dual-site Langmuir-Freundlich parameter fits for CO_2 in NTU-65 at various temperatures *T*.

T	$q_{A,sat}$	b_A	ν_A	$q_{B,sat}$	b_B	ν_B
K	mol kg^{-1}	$Pa^{-\nu A}$	dimensionless	mol kg^{-1}	$Pa^{-\nu B}$	dimensionless
263	0.2	2.7196E-04	0.85	3	1.1266E-64	13.3
273	0.87	4.116E-05	0.76	4	6.55E-105	21
283	2.5	9.640E-07	1			
298	0.2	9.640E-06	1			
333	0.2	3.0E-06	1			

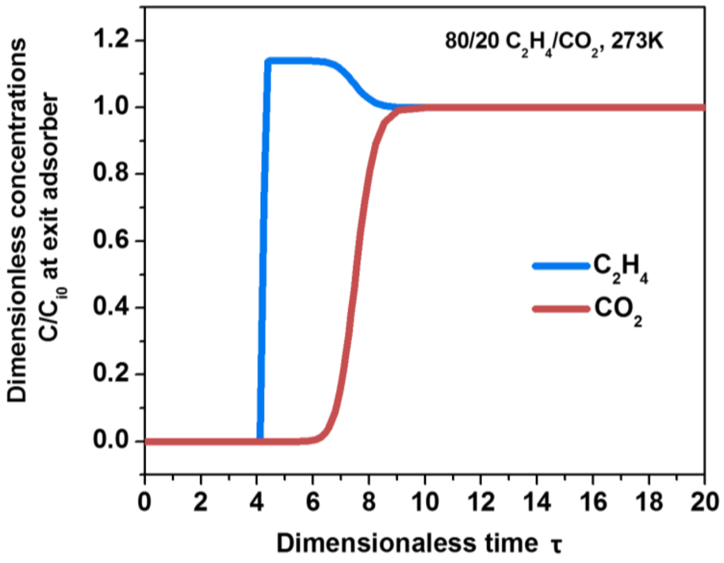

Figure S30. Transient breakthrough simulations for separation of 2-component C_2H_4/CO_2 mixtures using NTU-65 at 273 K, with partial pressures of 20 and 80 kPa for each component.

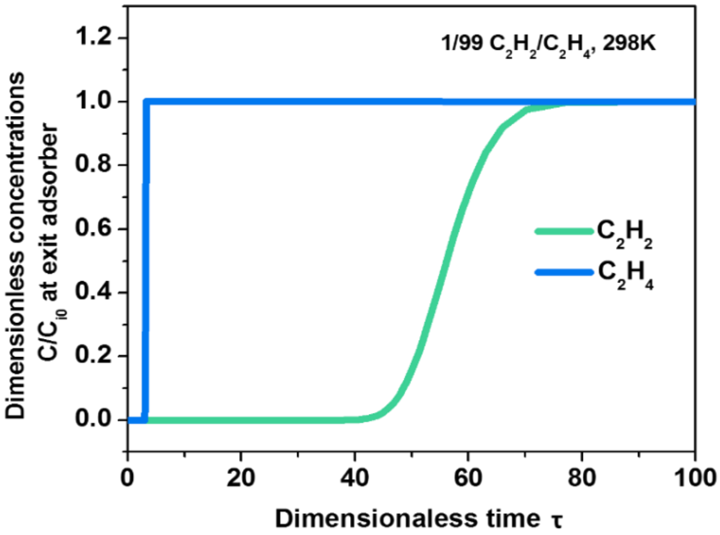

Figure S31. Transient breakthrough simulations for separation of 2-component C_2H_2/C_2H_4 mixtures using NTU-65 at 298 K, with partial pressures of 1 and 99 kPa for each component.

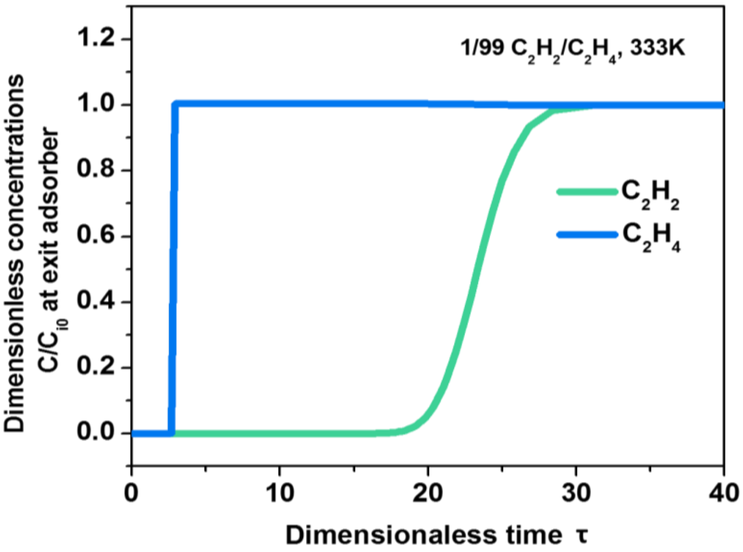

Figure S32. Transient breakthrough simulations for separation of 2-component C_2H_2/ C_2H_4 mixtures using NTU-65 at 333 K, with partial pressures of 1 and 99 kPa for each component.

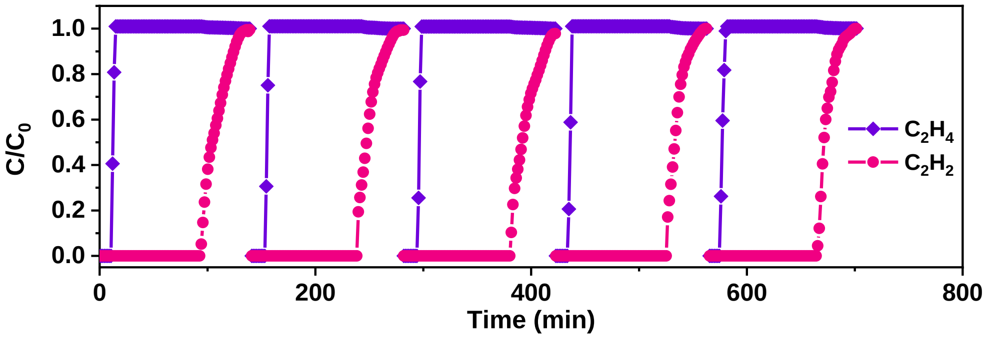

Figure S33. Five cycling of C_2H_2/C_2H_4 (1/99; v/v) breakthrough at 263 K by NTU-65.

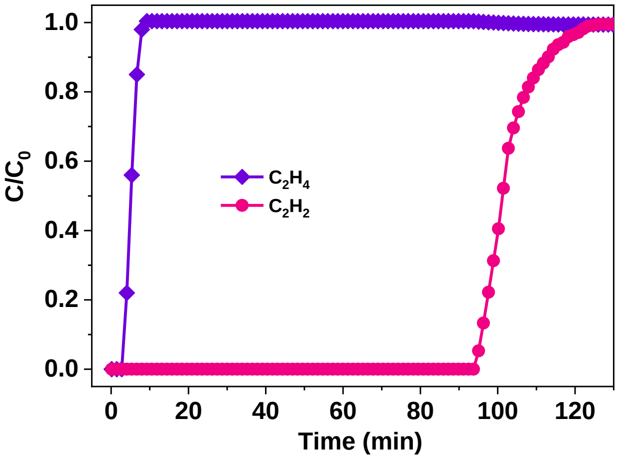

Figure S34. Breakthrough curve of C_2H_2/C_2H_4 (1/99; v/v) at 298 K by NTU-65.

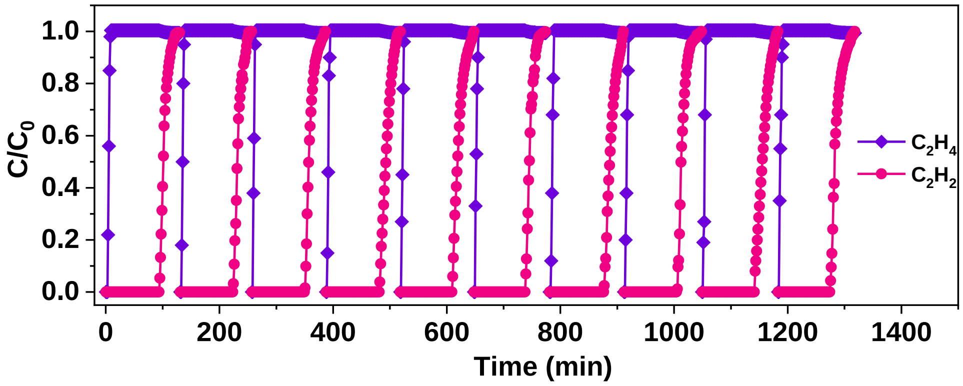

Figure S35. Ten cycling of C_2H_2/C_2H_4 (1/99; v/v) breakthrough at 298 K by NTU-65.

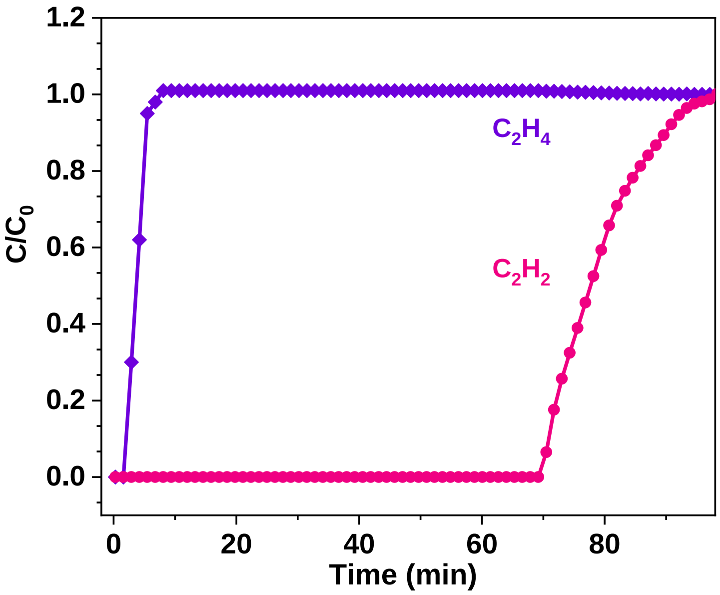

Figure S36. Breakthrough curve of C_2H_2/C_2H_4 (1/99; v/v) at 333 K by NTU-65.

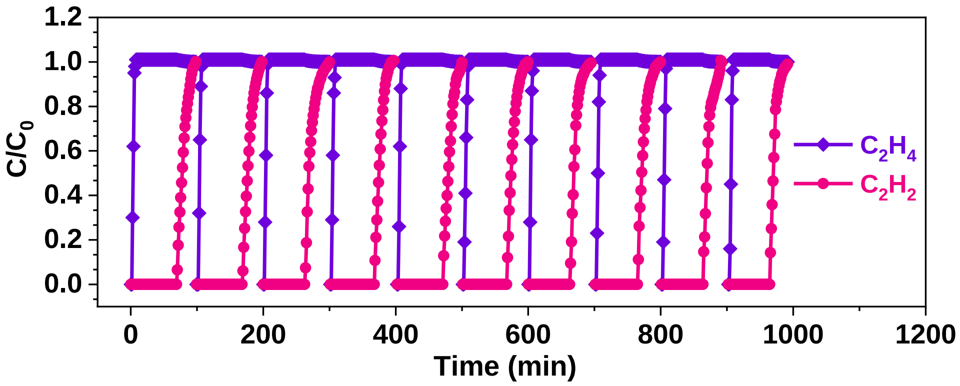

Figure S37. Ten cycling of C_2H_2/C_2H_4 (1/99; v/v) breakthrough at 333 K by NTU-65.

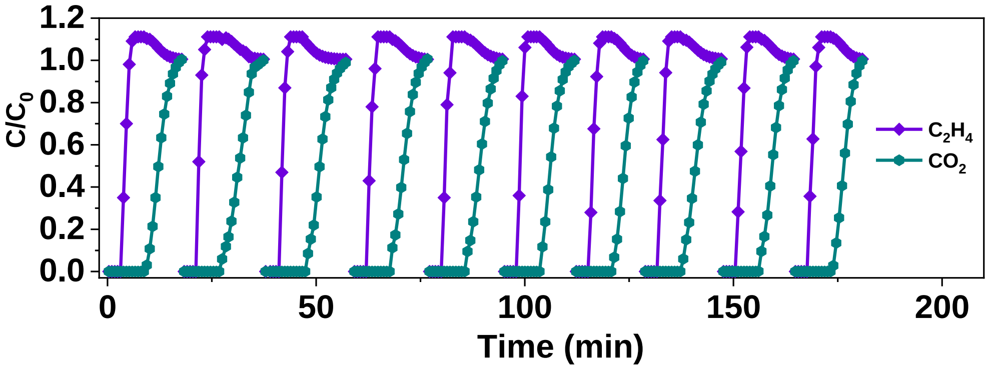

Figure S38. Ten cycling of CO_2/C_2H_4 (10/90; v/v) breakthrough at 263 K by NTU-65.

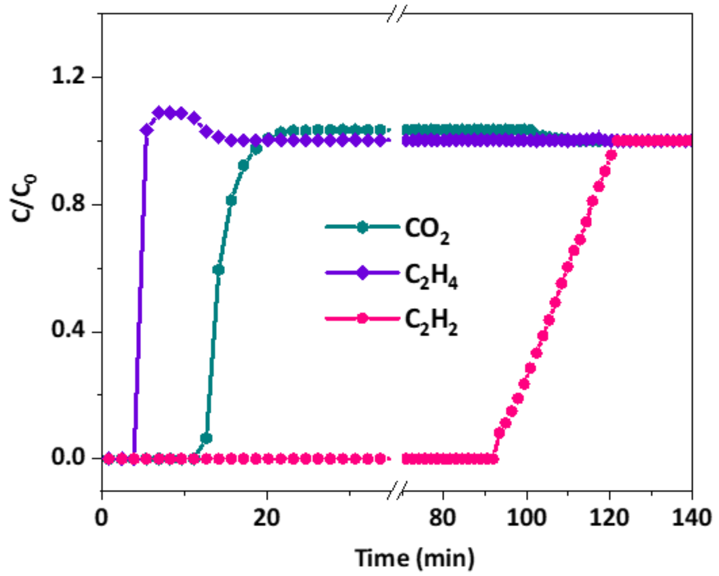

Figure S39. Breakthrough separation of ternary $C_2H_4/C_2H_2/CO_2$ (95.7/0.967/3.33, v/v/v) mixture at 263 K by NTU-65 (0.6859 g). The total pressure for all experiments is 1 bar, and the gas velocity is 3 mL·min^{-1}.

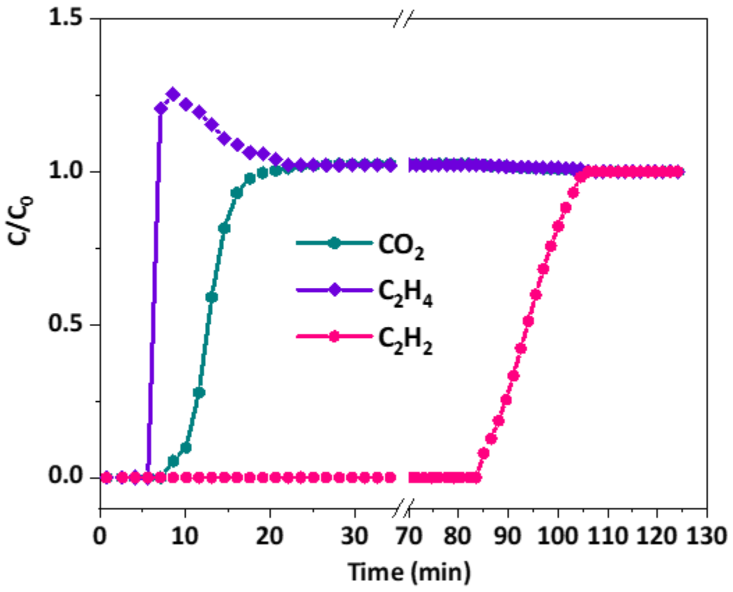

Figure S40. Breakthrough separation of ternary $C_2H_4/C_2H_2/CO_2$ (66.00/0.67/33.33, v/v/v) mixture at 263 K by NTU-65 (0.6859 g). The total pressure for all experiments is 1 bar, and the gas velocity is 3 mL·min^{-1}.

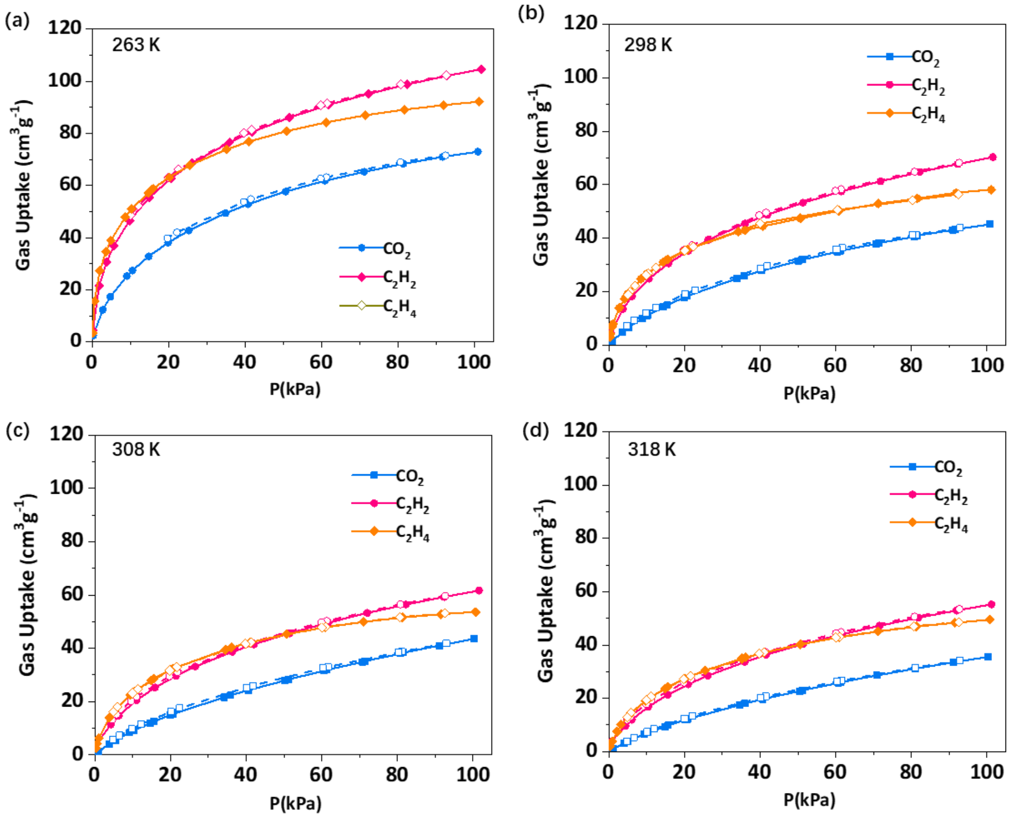

Figure S41. Adsorption and desorption isotherms of activated carbon at different temperatures.

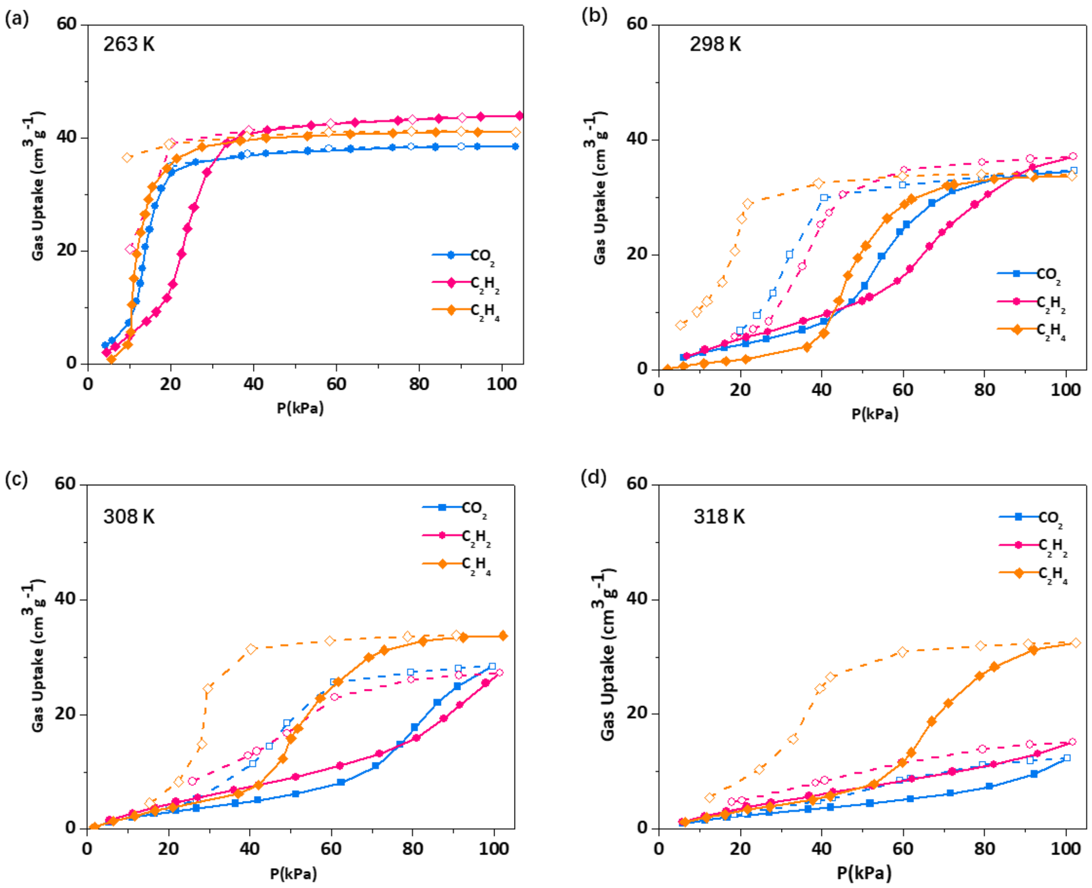

Figure S42. Adsorption and desorption isotherms of ZIF-7 at different temperatures.

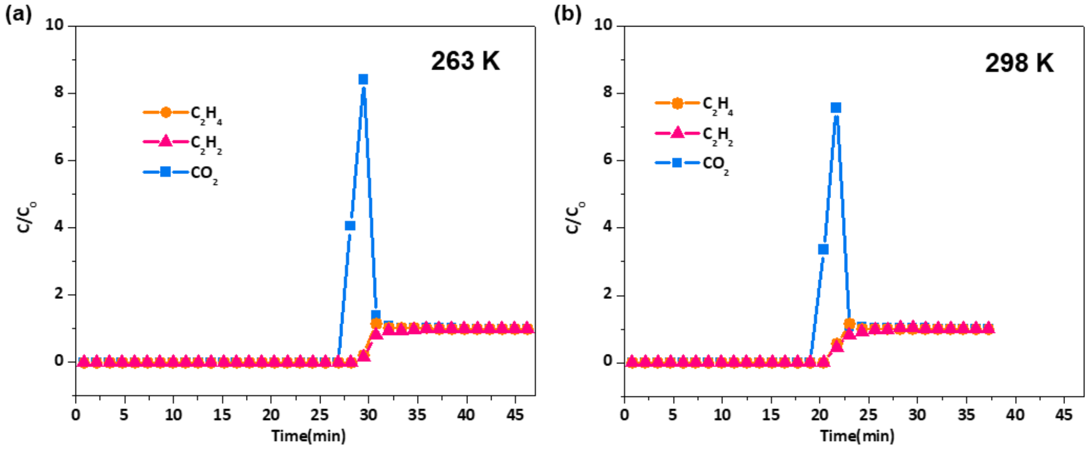

Figure S43. Breakthrough separation of ternary $C_2H_4/C_2H_2/CO_2$ (90/1/9, v/v/v) mixture by activated carbon at 263 K (a) and 298 K (b). The total pressure for all experiments is 1 bar, and the gas velocity is 3 mL·min^{-1}.

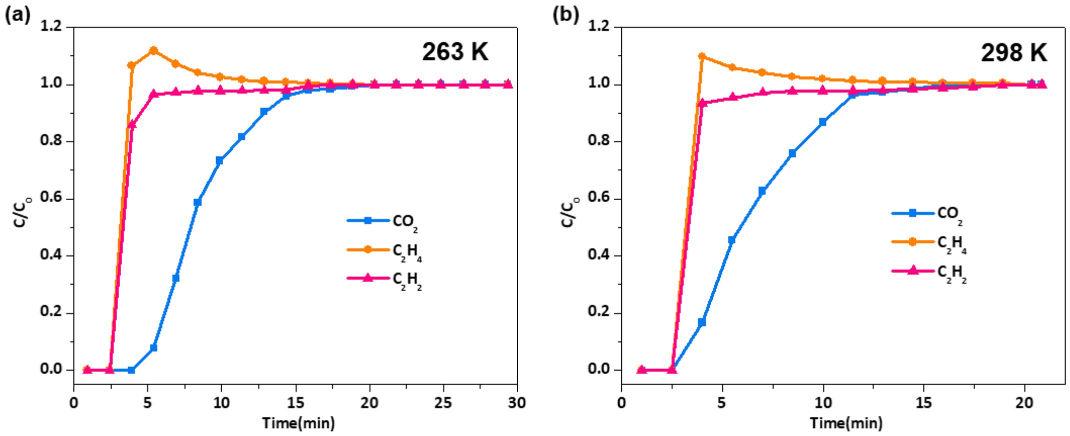

Figure S44. Breakthrough separation of ternary $C_2H_4/C_2H_2/CO_2$ (90/1/9, v/v/v) mixture by ZIF-7 at 263 K (a) and 298 K (b). The total pressure for all experiments is 1 bar, and the gas velocity is 3 mL·min^{-1}.

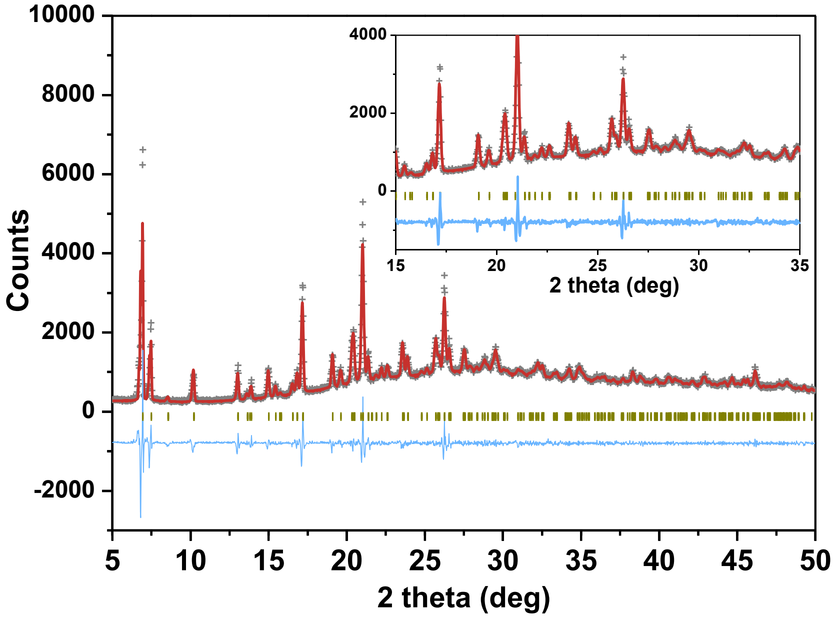

Figure S45. The results of LeiBail analysis for the PXRD of water treated **NTU-65** (60 days, room temperature). The wavelength of an incident X-ray is 1.0 Å. Refined parameters and reliability factors are as follows: a = 12.8289 Å; b = 25.4715 Å; c = 13.4210 Å, β = 118.4560º, R_p: 0.0475, R_{wp}: 0.0931.

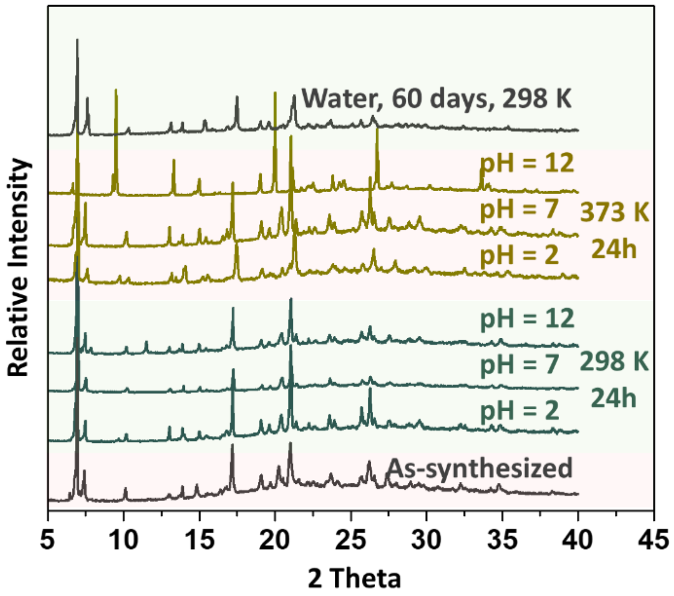

Figure S46. PXRD of NTU-65 after treatment of aqueous solution of different pH and temperature.

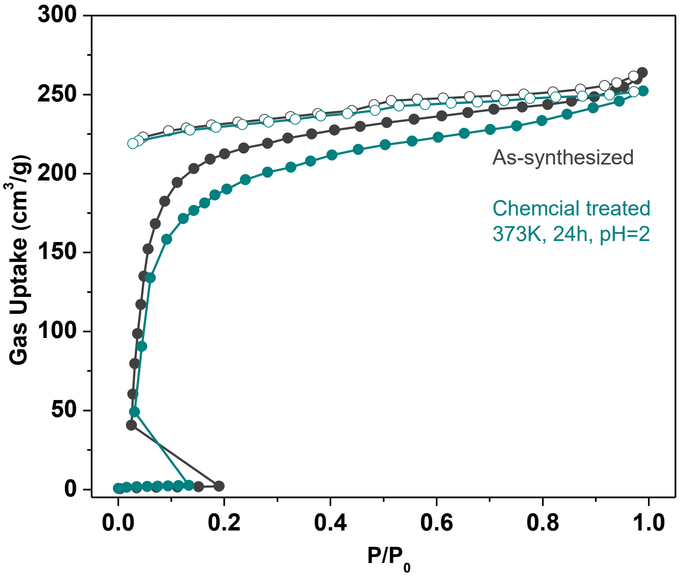

Figure S47. N_2 adsorption isotherms (77 K) of NTU-65 after treatment by aqueous solution pH=2 at 373 K for 24 h.

References

1. Sheldrick, G. M., A short history of SHELX. *Acta Crystallogr. Sec. A* **2008,** *64*, 112-122.
2. Spek, A. L., *PLATON, A Multipurpose Crystallographic Tool (Utrecht University,2001).*
3. Vandersluis, P.; Spek, A. L., Bypass - an Effective Method for the Refinement of Crystal-Structures Containing Disordered Solvent Regions. *Acta Crystallogr. Sec. A* **1990,** *46*, 194-201.
4. Krishna, R., The Maxwell-Stefan description of mixture diffusion in nanoporous crystalline materials. *Microporous Mesoporous Mater.* **2014,** *185*, 30-50.

5. Krishna, R., Methodologies for Evaluation of Metal-Organic Frameworks in Separation Applications. *RSC Advances* **2015,** *5*, 52269-52295.

6. Krishna, R., Screening Metal-Organic Frameworks for Mixture Separations in Fixed-Bed Adsorbers using a Combined Selectivity/Capacity Metric. *RSC Advances* **2017,** *7*, 35724-35737.

7. Krishna, R., Methodologies for Screening and Selection of Crystalline Microporous Materials in Mixture Separations. *Sep. Purif. Technol.* **2018,** *194*, 281-300.

8. Park, K. S.; Ni, Z.; Cote, A. P.; Choi, J. Y.; Huang, R. D.; Uribe-Romo, F. J.; Chae, H. K.; O'Keeffe, M.; Yaghi, O. M., Exceptional chemical and thermal stability of zeolitic imidazolate frameworks. *Proc. Natl. Acad. Sci. U. S. A.* **2006,** *103* (27), 10186-10191.

9. Bae, Y. S.; Lee, C. Y.; Kim, K. C.; Farha, O. K.; Nickias, P.; Hupp, J. T.; Nguyen, S. T.; Snurr, R. Q., High Propene/Propane Selectivity in Isostructural Metal-Organic Frameworks with High Densities of Open Metal Sites. *Angew. Chem. Int. Ed.* **2012,** *51* (8), 1857-1860.

10. Nugent, P.; Belmabkhout, Y.; Burd, S. D.; Cairns, A. J.; Luebke, R.; Forrest, K.; Pham, T.; Ma, S. Q.; Space, B.; Wojtas, L.; Eddaoudi, M.; Zaworotko, M. J., Porous materials with optimal adsorption thermodynamics and kinetics for CO2 separation. *Nature* **2013,** *495* (7439), 80-84.

11. Kresse G, Furthmuller J. Efficient iterative schemes for ab initio total-energy calculations using a plane-wave basis set. *Phys Rev B* 1996, **54**(16)**:** 11169-11186.

12. Dudarev SL, Botton GA, Savrasov SY, Humphreys CJ, Sutton AP. Electron-energy-loss spectra and the structural stability of nickel oxide: An LSDA+U study. *Phys Rev B* 1998, **57**(3)**:** 1505-1509.

13. Wang L, Maxisch T, Ceder G. Oxidation energies of transition metal oxides within the GGA+U framework. *Phy. Rev. B* 2006, **73**(19)**:** 195107-195112.

14. Grimme S, Ehrlich S, Goerigk L. Effect of the damping function in dispersion corrected density functional theory. *J. Comput. Chem.* 2011, **32**(7)**:** 1456-1465.

15. Kresse G, Joubert D. From ultrasoft pseudopotentials to the projector augmented-wave method. *Phys Rev B* 1999, **59**(3)**:** 1758-1775.

16. Perdew JP, Burke K, Ernzerhof M. Generalized gradient approximation made simple. *Phys. Rev. Lett.* 1996, **77**(18)**:** 3865-3868.

17. Monkhorst HJ, Pack JD. Special points for Brillouin-zone integrations. *Phys. Rev. B* 1976, **13**(12)**:** 5188-5192.